The Astrophysical Journal, 699:564–584, 2009 July 1 doi:10.1088/0004-637X/699/1/564

ATMOSPHERIC CIRCULATION OF HOT JUPITERS: COUPLED RADIATIVE-DYNAMICAL GENERAL CIRCULATION MODEL SIMULATIONS OF HD 189733b and HD 209458b

Adam P. Showman[1], Jonathan J. Fortney[2], Yuan Lian[1], Mark S. Marley[3], Richard S. Freedman[3,4], Heather A. Knutson[5], and David Charbonneau[5]

[1] Department of Planetary Sciences and Lunar and Planetary Laboratory, The University of Arizona, 1629 University Blvd., Tucson, AZ 85721, USA; showman@lpl.arizona.edu
[2] Department of Astronomy & Astrophysics, University of California, Santa Cruz, CA 95064, USA
[3] NASA Ames Research Center 245-3, Moffett Field, CA 94035, USA
[4] SETI Institute, 515 North Whisman Road, Mountain View, CA 94043, USA
[5] Harvard-Smithsonian Center for Astrophysics, 60 Garden Street, Cambridge, MA 02138, USA
Received 2008 September 7; accepted 2009 May 4; published 2009 June 12

ABSTRACT

We present global, three-dimensional numerical simulations of HD 189733b and HD 209458b that couple the atmospheric dynamics to a realistic representation of nongray cloud-free radiative transfer. The model, which we call the Substellar and Planetary Atmospheric Radiation and Circulation model, adopts the MITgcm for the dynamics and uses the radiative model of McKay, Marley, Fortney, and collaborators for the radiation. Like earlier work with simplified forcing, our simulations develop a broad eastward equatorial jet, mean westward flow at higher latitudes, and substantial flow over the poles at low pressure. For HD 189733b, our simulations without TiO and VO opacity can explain the broad features of the observed 8 and 24 μm light curves, including the modest day–night flux variation and the fact that the planet/star flux ratio peaks before the secondary eclipse. Our simulations also provide reasonable matches to the *Spitzer* secondary-eclipse depths at 4.5, 5.8, 8, 16, and 24 μm and the ground-based upper limit at 2.2 μm. However, we substantially underpredict the 3.6 μm secondary-eclipse depth, suggesting that our simulations are too cold in the 0.1–1 bar region. Predicted temporal variability in secondary-eclipse depths is $\sim$1% at *Spitzer* bandpasses, consistent with recent observational upper limits at 8 μm. We also show that nonsynchronous rotation can significantly alter the jet structure. For HD 209458b, we include TiO and VO opacity; these simulations develop a hot (>2000 K) dayside stratosphere whose horizontal dimensions are small at depth but widen with altitude. Despite this stratosphere, we do not reproduce current *Spitzer* photometry of this planet. Light curves in *Spitzer* bandpasses show modest phase variation and satisfy the observational upper limit on day–night phase variation at 8 μm.

Key words: atmospheric effects – methods: numerical – planets and satellites: general – planets and satellites: individual (HD 209458b, HD 189733b)

Online-only material: color figures

1. INTRODUCTION

Blasted by starlight 10^3–10^5 times stronger than that received by Jupiter and experiencing modest rotation rates due to their presumed tidal locking (Guillot et al. 1996), hot Jupiters occupy a fascinating meteorological regime that does not exist in our solar system (for an extensive review, see Showman et al. 2008b). Despite the wide range of transiting exoplanets that have been discovered, HD 189733b and HD 209458b remain the best-characterized hot Jupiters and represent important test cases for our understanding of these objects generally. A variety of observations now exist that constrain the three-dimensional temperature structure, composition, hazes, and albedo for these two planets. There is now hope that, by comparing these observations with detailed models, insights into this novel atmospheric regime can be achieved.

The strongest observational evidence for atmospheric motions comes from infrared (IR) light curves obtained with the *Spitzer Space Telescope*. Continuous light curves of HD 189733b over half an orbit have now been obtained at both 8 and 24 μm, constraining this planet's day–night heat transport (Knutson et al. 2007, 2009). The inferred dayside and nightside brightness temperatures are $\sim$1250 K and $\sim$1000 K, respectively.[6] Because the nightside temperatures would be extremely cold ($\sim$200 K) in the absence of winds, these observations imply the existence of a vigorous atmospheric circulation that efficiently transports heat from dayside to nightside. Further evidence for winds is the fact that the peak flux in both light curves occurs *before* secondary eclipse, implying that the hottest region lies 20°–30° of longitude east of the substellar point (Knutson et al. 2007, 2009). For HD 209458b, current data contain insufficient temporal sampling to determine whether similar offsets exist but nevertheless demonstrate that the 8 μm day–night brightness temperature difference is also modest (Cowan et al. 2007).

For both planets we now also have dayside photometry at all *Spitzer* broadband channels (centered at 3.6, 4.5, 5.8, 8.0, 16, and 24 μm), placing constraints on dayside composition and vertical temperature profile. These data were obtained by differencing the photometry of star+planet taken just before/after secondary eclipse from photometry taken during secondary eclipse, when only the star is visible. When compared with one-dimensional atmosphere models, these data suggest that, near the photosphere pressures, the dayside temperature of HD 189733b decreases with altitude (Charbonneau et al. 2008; Barman 2008; Knutson et al. 2009), whereas HD 209458b instead contains a thermal inversion (a hot stratosphere; Knutson et al. 2008; Burrows et al. 2007).

Following pioneering work by Hubeny et al. (2003), Fortney et al. (2008) and Burrows et al. (2008) suggested that hot Jupiters subdivide into two classes depending on whether or not their

[6] At 8 μm, the dayside and nightside brightness temperatures are 1258 $\pm$ 11 K and 1011 $\pm$ 51 K. At 24 μm, the dayside and nightside brightness temperatures are 1220 $\pm$ 47 K and 984 $\pm$ 48 K.

atmospheres contain highly absorbing substances such as gaseous TiO and VO. For a Sun-like primary, solar-composition planetary atmospheres inward of 0.04–0.05 AU are hot enough to contain TiO and VO; because of the extreme visible-wavelength opacity of these compounds, such planets absorb starlight at low pressure (∼mbar) and naturally exhibit dayside stratospheres. For planets outward of ∼0.05 AU, temperatures drop sufficiently for TiO and VO to condense in the deep atmospheres; these planets absorb starlight deeper in the atmosphere, lack stratospheres, and show spectral bands in absorption. Based on simple comparisons of radiative and advective timescales, Fortney et al. (2008) further suggested that the former category (dubbed "pM" class planets) would exhibit large day–night temperature differences, whereas the latter category ("pL" class) would exhibit more modest temperature contrasts. Their calculations suggest that HD 189733b is a pL-class planet while HD 209458b is a pM-class planet. This dichotomy makes these two planets a particularly interesting pair for comparison.

Given these developments, there is a pressing need for three-dimensional calculations of the atmospheric circulation on hot Jupiters. Several groups have investigated a range of two-dimensional and three-dimensional models (Showman & Guillot 2002; Cho et al. 2003, 2008; Cooper & Showman 2005, 2006; Showman et al. 2008a, 2008b; Langton & Laughlin 2007, 2008; Dobbs-Dixon & Lin 2008). However, to date, all published models have adopted severe approximations to the radiative transfer or excluded radiative heating/cooling entirely. While such simplified approaches are invaluable for investigating the underlying dynamics, a detailed attempt to explain wavelength-dependent photometry and light curves must include a realistic coupling of the radiative transfer to the dynamics.

Here, we present new numerical simulations that couple a realistic representation of nongray cloud-free radiative transfer to the dynamics. Surprisingly, coupling of three-dimensional dynamics to nongray radiative transfer has never previously been done for any giant planet, not even Jupiter, Saturn, Uranus, and Neptune. This is the first three-dimensional dynamical model for any giant planet—inside our solar system or out—to do so. We dub our model the Substellar and Planetary Atmospheric Radiation and Circulation model, or the SPARC model, and to honor its dynamical heritage usually refer to it as SPARC/MITgcm. Section 2 presents the model. Section 3 describes the basic circulation regime and resulting light curves and spectra for HD 189733b. Section 4 describes the effect of a nonsynchronous rotation rate, Section 5 considers HD 209458b, and Section 6 concludes.

2. MODEL

In the absence of dynamics, radiative transfer drives temperatures toward radiative equilibrium, which for a tidally locked irradiated planet means hot on the dayside and cold on the nightside. These thermal contrasts produce horizontal pressure gradients that generate winds, which drive the atmosphere away from radiative equilibrium. Because of this dynamical response, the radiative heating/cooling rate is nonzero, and it is this heating/cooling rate that drives the dynamics. In our previous work, we calculated the heating rate using a simplified Newtonian relaxation scheme (Showman & Guillot 2002; Cooper & Showman 2005, 2006; Showman et al. 2008a), but here we instead self-consistently calculate the heating rate from the radiative transfer. Figure 1 illustrates the coupling between dynamics and radiation in SPARC/MITgcm.

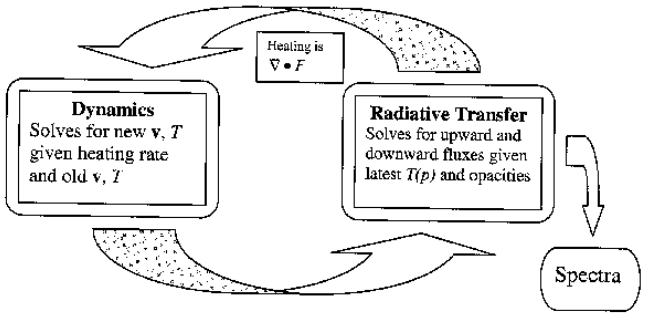

Figure 1. Coupled interrelationship between dynamics and radiation in our general circulation model (GCM), the SPARC/MITgcm. Spectra are calculated offline from GCM output.

2.1. Dynamics

We solve the global, three-dimensional primitive equations in spherical geometry using the MITgcm (Adcroft et al. 2004), which is a state-of-the-art atmosphere and ocean circulation model maintained at the Massachusetts Institute of Technology. The primitive equations are the standard equations for atmospheric flows in statically stable atmospheres when the horizontal dimensions greatly exceed the vertical dimensions. For HD 189733b and HD 209458b, with horizontal dimensions of 10^7–10^8 m and scale heights of ∼200 km and 500 km, respectively, we expect aspect ratios of ∼20–500. Showman et al. (2008a, 2008b) provide a more detailed discussion. The horizontal momentum, vertical momentum, continuity, and thermodynamic energy equations are

$$\frac{d\mathbf{v}}{dt} = -\nabla\Phi - f\mathbf{k}\times\mathbf{v} + \mathcal{D}_\mathbf{v}, \tag{1}$$

$$\frac{\partial\Phi}{\partial p} = -\frac{1}{\rho}, \tag{2}$$

$$\nabla\cdot\mathbf{v} + \frac{\partial\omega}{\partial p} = 0, \tag{3}$$

$$\frac{dT}{dt} = \frac{q}{c_p} + \frac{\omega}{\rho c_p} + \mathcal{D}_T, \tag{4}$$

where **v** is the horizontal velocity on constant-pressure surfaces, $\omega \equiv dp/dt$ is the vertical velocity in pressure coordinates, Φ is the gravitational potential on constant-pressure surfaces, $f \equiv 2\Omega\sin\phi$ is the Coriolis parameter, Ω is the planetary rotation rate (2π over the rotation period), **k** is the local vertical unit vector, q is the thermodynamic heating rate ($\mathrm{W\,kg^{-1}}$), and T, ρ, and c_p are the temperature, density, and specific heat at constant pressure, respectively. ∇ is the horizontal gradient evaluated on constant-pressure surfaces, and $d/dt = \partial/\partial t + \mathbf{v}\cdot\nabla + \omega\partial/\partial p$ is the material derivative. Curvature terms are included in $\mathbf{v}\cdot\nabla\mathbf{v}$. Equation (4) is actually solved in an alternate form,

$$\frac{d\theta}{dt} = \frac{\theta}{T}\frac{q}{c_p} + \mathcal{D}_\theta, \tag{5}$$

where $\theta = T(p/p_0)^\kappa$ is the potential temperature (a measure of entropy), κ is the ratio of gas constant to specific heat at constant pressure, and p_0 is a reference pressure (here chosen to be 1 bar, but note that the dynamics are independent of the choice of p_0). The dependent variables **v**, ω, Φ, ρ, θ, and T are functions of longitude λ, latitude ϕ, pressure p, and time t. In

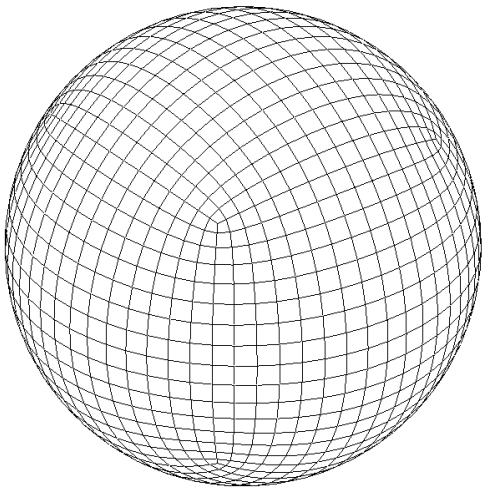

Figure 2. Cubed-sphere grid at a resolution of C16 (i.e., 16 × 16 elements per cube face), roughly equivalent to a global resolution of 64 × 32 in longitude and latitude.

the above equations, the quantities $\mathcal{D}_{\mathbf{v}}$, $\mathcal{D}_T$, and $\mathcal{D}_\theta$ represent additional source/sink terms beyond those described explicitly in the equations (see below).

The MITgcm has been widely used in the atmospheric and ocean-science communities and has been successfully benchmarked against standard test cases (Held & Suarez 1994). The model, with simplified forcing, has also shown success in reproducing the global circulations of giant planets in our solar system (Lian & Showman 2008).

The MITgcm solves the equations on a staggered Arakawa C grid (Arakawa & Lamb 1977) using a finite-volume discretization. Two coordinate systems are supported: the standard longitude/latitude coordinate system and a curvilinear coordinate system called the "cubed sphere," shown in Figure 2. In the longitude/latitude system, the east–west (zonal) grid spacing converges to zero near the poles. This convergence implies, via the Courant–Fredricks–Levy (CFL) constraint, that the timestep must approach zero to maintain numerical stability. This difficulty can be surmounted using a polar filter that smooths the east–west variability of the dynamical fields near the poles, which increases the effective grid size and allows the use of a finite timestep. In contrast, the cubed-sphere grid lacks the singularities at the poles and thereby sidesteps this problem. The price is a non-orthogonal grid and the existence of eight special "corner points" (three of which can be seen in Figure 2). Unlike the situation at the poles in a longitude/latitude grid, however, the coordinate lines in the cubed-sphere grid remain well separated until very close to the corner points; depending on resolution, the size of finite-volume elements abutting the corners is typically one-half to one-third of that away from the corners. The upshot is that one can typically use a longer timestep with the cubed-sphere grid than a longitude/latitude grid at comparable resolution. The simulations presented here adopt the cubed-sphere grid.

The top boundary condition is zero pressure and the bottom boundary condition is an impermeable surface, which we place far below the region of interest. Both boundaries are free slip in horizontal velocity. We explore horizontal resolutions of C16, C32, and C64 (implying that each of the six "cube faces" has a resolution of 16 × 16, 32 × 32, and 64 × 64 finite-volume elements, respectively); these roughly translate to global resolutions of 64 × 32, 128 × 64, and 256 × 128 in longitude and latitude. For a model with N_L vertical layers, the bottom $N_L - 1$ layers have interfaces that are evenly spaced in log pressure between $p_{\rm top}$ and the basal pressure; the top layer extends from a pressure of zero to $p_{\rm top}$. In most simulations, we place the bottom boundary at 200 bars, safely below the active meteorology near the photosphere. We generally place $p_{\rm top}$ at 0.2 mbar or 2 μbar, using 40 or 53 layers, respectively; in both cases, this resolves each pressure scale height with 2.9 layers.

We adopt the third-order Adams–Bashforth timestepping scheme (Durran 1991), which has favorable properties over the more commonly used leapfrog scheme. To maintain numerical stability, we apply a fourth-order Shapiro filter to the time derivatives of $\mathbf{v}$ and θ at each timestep. This source/sink, which is represented by the terms $\mathcal{D}_{\mathbf{v}}$ and $\mathcal{D}_\theta$ in the governing equations, is analogous to a hyperviscosity: it horizontally smooths grid-scale variations while leaving long-wavelength structures relatively unaffected.

CFL constraints limit us to a short dynamical timestep; for our C16, C32, and C64 simulations, we generally use 50 s, 25 or 15 s, and 6 s, respectively.

In our nominal simulations, we assume the planets rotate synchronously with their orbital periods, implying rotation periods of 2.2 days ($\Omega = 3.278 \times 10^{-5}\,{\rm s}^{-1}$) for HD 189733b and 3.5 days ($\Omega = 2.078 \times 10^{-5}\,{\rm s}^{-1}$) for HD 209458b. Nevertheless, because deviations from synchronous rotation are possible (e.g., Showman & Guillot 2002), we also ran some simulations with differing rotation periods. We adopt gravity and planetary radius of $21.4\,{\rm m\,s}^{-2}$ and 8.2396×10^7 m for HD 189733b and $9.36\,{\rm m\,s}^{-2}$ and 9.437×10^7 m for HD 209458b. The equation of state is ideal gas. We fix $c_p = 1.3 \times 10^4\,J\,{\rm kg}^{-1}\,{\rm K}^{-1}$ and use $\kappa = 2/7$, appropriate to a predominantly hydrogen atmosphere, for both planets. In most cases, the initial condition contains no winds and adopts an initial temperature profile from a one-dimensional planetwide-average radiative-equilibrium calculation.

As discussed by Showman et al. (2008b) and Goodman (2009), the mean winds that develop in an atmosphere depend in principle not only on forcing but also on damping processes that remove kinetic and/or potential energy. For solar-system planets, kinetic energy loss occurs via turbulence, wave breaking, and friction against the surface (if any). In the deep interior of gas giants ($p \gtrsim 10^5$ bars), Ohmic dissipation may also provide an important source of drag (Kirk & Stevenson 1987; Liu et al. 2008), although it is unclear whether the atmospheric circulation on hot Jupiters couples to such deep regions. Rigorously representing such frictional effects in numerical models is difficult, however; the turbulence associated with small-scale shear instabilities and wave breaking often has length scales much smaller (by up to several orders of magnitude) than can easily be resolved in global three-dimensional numerical models. In Earth GCMs, these dissipative processes are generally parameterized by adding to the equations empirical damping terms (e.g., a vertical diffusion to represent kinetic energy losses by subgrid-scale shear instabilities and waves). A difficulty is that such prescriptions, while physically motivated, are generally non-rigorous and the extent to which they can be extrapolated to hot Jupiters is unclear. Moreover, simulations of the cloud-level circulation on Jupiter, Saturn, Uranus, and Neptune that lack frictional drag parameterizations have nevertheless shown success in reproducing the qualitative features of the observed flow on these planets (e.g., Scott & Polvani 2007, 2008; Showman 2007; Lian & Showman 2008, 2009). Therefore, while recognizing the possible importance that frictional processes could play for hot

Jupiters, for the present study we do not include frictional damping terms in the momentum equation (Equation (1)) other than the Shapiro filter, which causes a diffusive damping of small-scale wind structures. Once our simulations have spun up, this implies that, except for energy losses due to the Shapiro filter, the globally integrated rate of production of available potential energy (APE; see Peixoto & Oort 1992, Chapter 14) and its net conversion to kinetic energy (KE) become modest, with the potential-to-kinetic energy conversion in some regions of the atmosphere being counteracted by the kinetic-to-potential energy conversion in other regions.[7] In a future study, we will explore the influence that plausible frictional parameterizations exert on the wind speeds and circulation geometry.

Goodman (2009) suggested that the heating associated with frictional dissipation should be included in the thermodynamic energy equation. Our study, like previous published hot-Jupiter studies, does not include this effect; this is equivalent to assuming that any frictional heating is small compared to the radiative heating. This is typically a reasonable assumption for atmospheres: the globally averaged rate of kinetic energy production (and hence the rate at which that kinetic energy can be dissipated into thermal energy) is controlled by the thermodynamic efficiency of the atmospheric heat engine, which is typically much less than 100%, at least for atmospheres in the solar system. In this situation, the frictional heating is much less than the radiative heating. On Earth, for example, the globally averaged rate of frictional dissipation by the large-scale circulation is $2\,\mathrm{W\,m^{-2}}$, which is only a few percent of the latitude-dependent net radiative heating/cooling rate (Peixoto & Oort 1992). This implies that the frictional heating is only a small perturbation to the total heating rate. Because giant planets lack surfaces (which is the primary source of friction on Earth) it is plausible that the frictional damping, and the heating it causes, represents an even smaller effect on gas giants than terrestrial planets. Note that, to date, frictional heating has not been included in cloud-level atmosphere simulations of Jupiter, Saturn, Uranus, and Neptune. For hot Jupiters, given the considerable uncertainty arising from other factors (e.g., uncertainties in opacities, composition, possible presence of clouds/hazes, and possible nonsynchronous rotation, all of which influence the circulation), it seems reasonable to neglect this effect for the present.

2.2. Radiative Transfer Calculation

We coupled the MITgcm to the plane-parallel radiative-transfer code of Marley & McKay (1999), which is a state-of-the-art model that has been extensively used in one-dimensional investigations of Titan, the giant planets, brown dwarfs, and exoplanets (e.g., McKay et al. 1989; Marley et al. 1996, 1999, 2002; Burrows et al. 1997; Fortney et al. 2005, 2006a, 2006b, 2008; Fortney & Marley 2007; Saumon & Marley 2008). We here use the code in its two-stream formulation, allowing treatment of the upward and downward radiative fluxes versus wavelength and height throughout the three-dimensional grid. Multiple scattering is properly accounted for.

[7] For example, our simulations develop a broad eastward equatorial jet; near-IR photosphere levels, where this jet transports air from day-to-night, the air generally flows in the same direction as the horizontal pressure-gradient force (i.e., $\mathbf{v} \cdot \nabla\Phi < 0$), so potential energy is converted to kinetic energy. However, where the jet transports air from night-to-day, such a jet tends to flow against the horizontal pressure-gradient force ($\mathbf{v} \cdot \nabla\Phi > 0$), so kinetic energy is converted to potential energy. In a global mean, there is a large degree of cancellation between these competing effects.

Table 1
Opacity Bins

Wavelength (μm)	Wavelength (μm)
324.68	46.00
46.00	20.00
20.00	10.40
10.40	6.452
6.452	5.220
5.220	4.400
4.400	3.800
3.800	3.288
3.288	2.989
2.989	2.505
2.505	2.170
2.170	2.020
2.020	1.777
1.777	1.593
1.593	1.497
1.497	1.330
1.330	1.197
1.197	1.100
1.100	1.005
1.005	0.960
0.960	0.910
0.910	0.860
0.860	0.785
0.785	0.745
0.745	0.675
0.675	0.612
0.612	0.572
0.572	0.495
0.495	0.400
0.400	0.261

Note. Opacity bins used in the radiative-transfer calculation. Each row lists the bounding wavelengths for one bin.

2.2.1. Opacities

The code treats opacities using the correlated-k method (Goody & Yung 1989), which is ideal for use in GCMs because it is fast and accurate. In this approach, opacities are first computed exactly at millions of individual frequency points at over 700 pressure–temperature (p–T) points, accounting for the influence of all molecular and atomic lines in our opacity database (Freedman et al. 2008). Line broadening is computed for each line of each species at each pressure–temperature point. The summed opacities at each p–T point thus account for both the relative abundances of each absorbing species as well as the line shapes appropriate for the particular physical conditions. The spectrum of opacities is then divided into 30 frequency bins[8] as listed in Table 1.

The opacities at each of the several tens of thousands of frequency points within each frequency bin (Table 1) are then sorted by strength and described statistically thus enabling Gaussian integration to be used to solve for the radiative fluxes through the model eight times, once for each probability interval within each spectral bin. The model flux within each of the 30 frequency bins is the sum of the flux calculations weighted by the relative contribution of each statistical opacity interval. By

[8] In recent one-dimensional applications of our code, we typically use 196 intervals (e.g., Fortney et al. 2005, 2006a, 2006b, 2008). Extensive testing has revealed that, for a specified $T(p)$ profile, the net radiative flux calculated using 30 bins differs less than 1% from that calculated using 196 and is substantially faster in the GCM environment.

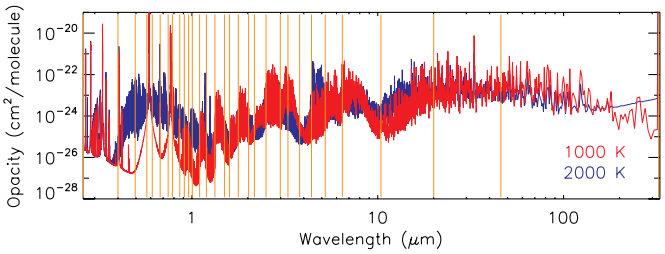

Figure 3. Opacity (in cm^2 $molecule^{-1}$) vs. wavelength at $p = 1$ bar and $T = 1000$ K (red) and 2000 K (blue) assuming solar composition (modified for rainout where appropriate) including TiO and VO. In the mid-IR, much of the structure results from H_2O, CO, and (at 1000 K) CH_4; the two prominent Na lines are evident in the visible in the 1000 K case. Significant additional visible-wavelength opacity occurs in the 2000 K case due to absorption by TiO and VO. Wavelength boundaries for the 30 opacity bins in our GCM runs are shown with vertical orange lines and listed numerically in Table 1.

(A color version of this figure is available in the online journal.)

using two intervals (one for the opacities weaker than 95% of the highest value and one for the strongest 5%), each with four Gauss points (for eight total Gauss points), we resolve both the important strongest lines as well as the background continuum within each bin. This *k*-coefficient approach has been widely used in planetary atmosphere calculations for over two decades and is frequently employed in GCM calculations. The method is subject to significant errors only when the distribution of opacity within a single spectral bin varies substantially with height in the atmosphere as might happen if one absorber is replaced by another with a very different opacity shape (for example, a strong red slope within a bin replaced by a strong blue opacity slope *within that same bin*). In practice, such concerns are mitigated by careful choice of the opacity intervals. To compute the opacity at arbitrary *p*–*T* points, we interpolate within our grid of *k*-coefficients.

We chose the wavelength boundaries of our bins in an attempt to optimize a number of competing needs. We wish to have highest spectral resolution (narrowest bins) in the optical at the peak of the incident flux (to best resolve absorption of incident energy) and in the near-IR to similarly resolve the peak of the emergent flux. In addition, distinct bins should resolve important opacity peaks and valleys so that there is a relatively flat opacity distribution within each bin. This minimizes the dynamic range that must be covered by the eight *k*-coefficient Gauss points within each bin. Examples include the water opacity windows in the near-IR, the CO bandhead at 2.3 μm, and TiO in the optical. We also wish to minimize the total number of bins while still covering the entire spectral range from the UV to the thermal IR. Our choice of bins is listed in Table 1 and depicted graphically in Figure 3.

The opacities themselves are computed from a comprehensive opacity database (Freedman et al. 2008), calculated assuming local thermodynamic and chemical equilibrium (Lodders & Fegley 2002, 2006) as a function of *p*, *T*, and wavelength. We perform simulations with opacities corresponding to 1-, 5-, and 10-times-solar abundances (appropriately modified for rainout of condensed species whenever condensation should occur). For HD 189733b, the inferred water abundance (Tinetti et al. 2007; Swain et al. 2008b) is consistent with near-solar metallicity for both water and carbon (Showman 2008). For HD 209458b, Barman (2007)'s fits to transit data suggest abundances not exceeding a few times solar, while Sing et al. (2008)'s fits to transit data suggest two-times-solar sodium abundance.

TiO and VO deserve special mention. For our simulations of HD 189733b, we use opacity databases that exclude TiO and VO, consistent with secondary-eclipse data (Charbonneau et al. 2008), one-dimensional radiative-transfer studies (Barman 2008; Knutson et al. 2009), and evolution models suggesting that TiO and VO should sequester deeper than ~10–100 bars where solid clouds incorporating Ti and V form (e.g., Fortney et al. 2006b). For HD 209458b, however, the detection of a hot stratosphere (Knutson et al. 2008; Burrows et al. 2007), possibly associated with TiO and VO (Hubeny et al. 2003; Fortney et al. 2008) suggest that gaseous TiO and VO may exist in this planet's atmosphere. For HD 209458b, therefore, we run some cases that include gaseous TiO and VO and other cases that exclude them.

For simplicity, we neglect cloud opacities. This appears to be reasonable for HD 189733b, at least for emitted thermal radiation, since absorption features observed in transit spectra longward of ~1.5 μm (Tinetti et al. 2007; Swain et al. 2008b; Sing et al. 2008) indicate that gas rather than particles dominates the opacity along the slant transit path. The situation is less clear at visible wavelengths (Pont et al. 2008; Redfield et al. 2008), but submicron-sized haze particles are a possibility. In any event, because the *slant* optical depth exceeds the *normal* optical depth by a factor of ~50 (Fortney 2005), the data are nevertheless consistent with normal cloud optical depths $\ll 1$. Fewer constraints exist for HD 209458b. Some authors have suggested silicate absorption features in emission spectra (Richardson et al. 2007), but debate exists (Swain et al. 2008a).

2.2.2. Flux Calculation

We solve for the net flux through each level of a specified local atmospheric structure using two separate techniques: one for the incident stellar and one for the emitted planetary thermal radiation. This subdivision is common in planetary-atmosphere studies since the incident radiation is dominated by the direct stellar beam accompanied by a weaker but more uniform scattered flux while the thermal emitted radiation is comparatively much more uniform over a hemisphere, thus suggesting separate flux solution methods. For solar-system atmospheres, the solar and planetary fluxes usually occupy distinct spectral intervals. However, for hot extrasolar planets the incident and emitted fluxes substantially overlap near 1 μm and thus the net flux within a layer is the sum of the net stellar and thermal fluxes, which are computed by differing techniques within the same spectral interval.

For the incident stellar flux, we follow McKay et al. (1989) and Marley & McKay (1999) and employ the delta-discrete ordinates method (see Appendix I of McKay et al. 1989). We adopt stellar spectra from Kurucz (see http://hurucz.harvard.edu/stars.html) and assume that HD 189733b and HD 209458b have distances of 0.0313 and 0.046 AU from their stars, respectively. Obliquities and orbital eccentricities are assumed zero. Stellar fluxes are computed only in those bins lying shortwards of 6 μm.

For the thermal flux we follow the approach used in our brown dwarf work and employ the "two-stream source function" technique of Toon et al. (1989) which was specifically developed for rapid, accurate computation of radiative heating rates in inhomogeneous atmospheres. This approach is well suited for atmospheres with scattering cloud layers, which we will eventually include. The present implementation does include Rayleigh scattering, although this is generally unimportant for most of the thermal bins. The accuracy of this technique for various limiting cases is discussed in detail by Toon et al.

(1989). We model thermal radiation from the planet from 0.26 to 325 μm. Extensive experience with this technique employed with k-coefficient opacities in the context of brown dwarf atmospheres has shown that integrated fluxes usually agree to much better than 0.1% with fluxes computed using detailed line-by-line calculations.

In most one-dimensional radiative-transfer calculations, an iteration is performed to drive the solution into radiative equilibrium. Here, the three-dimensional solution is not in radiative equilibrium, and no iteration is needed. Instead, at each timestep, we pass a driver subroutine the most recent three-dimensional temperature field, consisting of numerous individual $T(p)$ columns, one per element in the horizontal grid. We loop over all these columns and, for each, we call the radiative-transfer solver once (without iteration) to determine the upward and downward fluxes versus frequency and pressure throughout that column. For each column, we include the appropriate incident starlight: columns on the nightside emit radiation but receive no starlight, while columns on the dayside receive starlight along an angle θ from the local vertical. The cosine of this angle, μ, varies from 1 at the substellar point to 0 at the terminator. Columns closer to the substellar point thus receive greater stellar flux, and this flux penetrates to greater pressures because of the shorter atmospheric path lengths.

2.3. Coupling Dynamics and Radiative Transfer

Once we calculate the wavelength-dependent radiative fluxes, we sum them to obtain the net vertical flux everywhere over the three-dimensional grid at that timestep. We then obtain the thermodynamic heating rate q (Equation (4)) as follows. If an atmospheric layer absorbs more (less) radiation than it emits, the layer experiences heating (cooling). The thermodynamic heating rate per unit volume ($\mathrm{W\,m^{-3}}$) is thus simply $-\partial F/\partial z$, where z is height and F is the net, wavelength-integrated flux. Expressed in pressure coordinates using hydrostatic balance, the heating rate per unit mass, q, becomes

$$q = g\frac{\partial F}{\partial p}. \tag{6}$$

This is then used to drive the dynamics via Equation (5); see Figure 1. Note that this expression neglects the heating contribution due to the horizontal divergence of the horizontal radiative flux, which is at least a factor of $\sim$30 less than that in Equation (6) for conditions relevant to hot Jupiters.

We use the same vertical gridding for the dynamics and radiative-transfer calculations. In the SPARC/MITgcm, the vertical grid is staggered such that T, θ, and horizontal wind are defined within the layers, while certain other quantities (such as vertical velocity) are defined at the interfaces between layers. Because q is used to update θ (Equation (5)), q should be computed within the layers so that it has the same vertical positioning as θ. To calculate q, we thus evaluate $\partial F/\partial p$ by finite differencing the fluxes and pressures between the *interfaces* that over- and underlie a given layer. This maximizes accuracy while positioning $\partial F/\partial p$ within the layer. Note that we use the same layer spacing in the dynamics and radiative transfer calculations; one-dimensional radiative transfer tests performed offline suggest that this vertical gridding is sufficient to resolve the radiative transfer.

As a test, we ran a suite of simulations where we turned off the dynamics. In these cases, the temperature profiles relaxed toward the expected radiative equilibrium (as defined by solutions generated with the radiative-equilibrium one-dimensional version of the radiation code) for the specified value of μ. This demonstrates that the calculation of the thermodynamic heating rate (Equation (6)) functions properly.

In most SPARC/MITgcm simulations, we update the radiative fluxes less frequently than the dynamical timestep. This is standard practice in GCMs and helps maintain computational efficiency. For our simulations without TiO and VO, we found that a radiative step of 500–1000 s was generally sufficient. For simulations with TiO and VO, however, a much shorter radiative timestep of 100 s or less was necessary to maintain numerical stability. For computational expediency, in some simulations, particularly our high-resolution cases, we perform radiative transfer only on every other grid column and interpolate the fluxes and heating rates in between.

SPARC/MITgcm output includes the emergent fluxes versus wavelength and position everywhere over the globe. However, because we run the GCM with only modest spectral resolution, we generally recalculate disk-averaged light curves and spectra offline at higher spectral resolution using the three-dimensional temperature fields following the procedure described in Fortney et al. (2006a) and Showman et al. (2008a). This procedure ensures that limb darkening is properly treated.

3. RESULTS: SYNCHRONOUSLY ROTATING HD 189733B

3.1. Circulation Regime

In our simulations, the imposed day–night irradiation gradient rapidly leads to the development of large day–night temperature contrasts and winds reaching several km $\mathrm{s^{-1}}$. A statistically steady flow pattern is achieved at pressures $<$1 bar after less than 100 Earth days of integration. Figures 4 and 5 illustrate the behavior for our nominal, synchronously rotating simulation of HD 189733b using solar opacities without TiO and VO. Figure 4 shows the temperature (colorscale) and winds (arrows) over the globe on three different pressure levels, while Figure 5 depicts the zonally averaged zonal wind[9] versus latitude and pressure.

As in our previous simulations with simplified forcing (Showman & Guillot 2002; Cooper & Showman 2005, 2006; Showman et al. 2008a), the flow becomes dominated by a superrotating (eastward) equatorial jet extending from latitudes of approximately 30°N to 30°S. Vertically, the jet remains coherent from the top of the model (0.2 mbar) to the $\sim$10 bar level and reaches peak zonal-mean zonal wind speeds of 3.5 $\mathrm{km\,s^{-1}}$ at pressures of 10–100 mbar (Figure 5). The latitudinal width and longitudinal structure of the jet depend strongly on altitude. Longitudinal variability in the jet speed is small at pressures exceeding $\sim$200 mbar but increases with altitude and exceeds 2 $\mathrm{km\,s^{-1}}$ at the top of the model, with the fastest eastward winds occurring in the hemisphere west of the substellar point and the slowest winds occurring near and east of the substellar point. The transition between these regions narrows with altitude, and at pressures less than a few mbar, the equatorial flow appears to pass through a hydraulic jump as it approaches the substellar point from the west (e.g., Figure 4, top panel), leading to a near-discontinuity in the zonal and meridional wind speed at longitudes of $-50°$ to $-80°$ (depending on latitude). Accompanying this structure are strong downward velocities, and the adiabatic compression associated with this descent leads to a

[9] In atmospheric dynamics, the terms zonal and meridional wind refer to the east–west and north–south wind, respectively (with eastward and northward being positive); a zonal average refers to an average of any quantity in longitude.

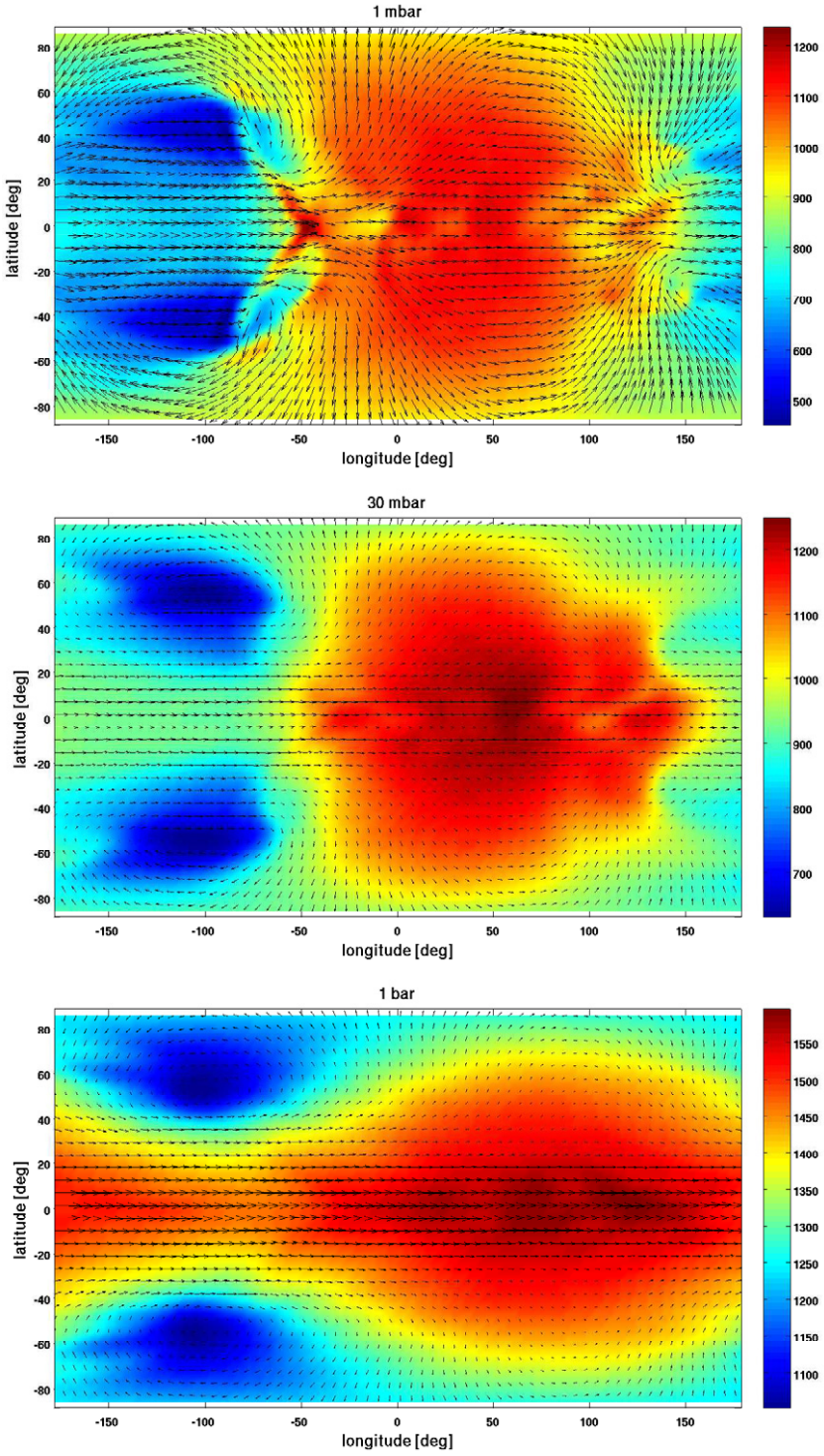

Figure 4. Temperature (colorscale, in K) and winds (arrows) for nominal HD 189733b simulation with solar abundances and no TiO/VO. Panels show flow at 1 mbar (top); 30 mbar, corresponding to an approximate photosphere level in the mid-IR (middle); and 1 bar (bottom). Resolution is C32 (roughly equivalent to a global horizontal resolution of 128 × 64 in longitude and latitude) with 40 vertical layers. Substellar point is at longitude, latitude (0°, 0°). Dayside is the region between longitudes −90° and 90°. Nightside is at longitudes −180° to −90° and 90° to 180°.

(A color version of this figure is available in the online journal.)

warm chevron-shaped structure in the temperature (Figure 4, top panel).

At higher latitudes (poleward of ∼45°), the zonal-mean zonal wind is westward at pressures <1 bar (Figure 5). Nevertheless, this high-latitude flow exhibits complex structure, with westward flow occurring west of the substellar point, eastward flow east of the substellar point, and substantial day-to-night flow over the poles. These polar flows indicate the importance of performing global simulations and would not be properly captured if the poles were removed from the computation domain, as done by some previous authors (Dobbs-Dixon & Lin 2008).

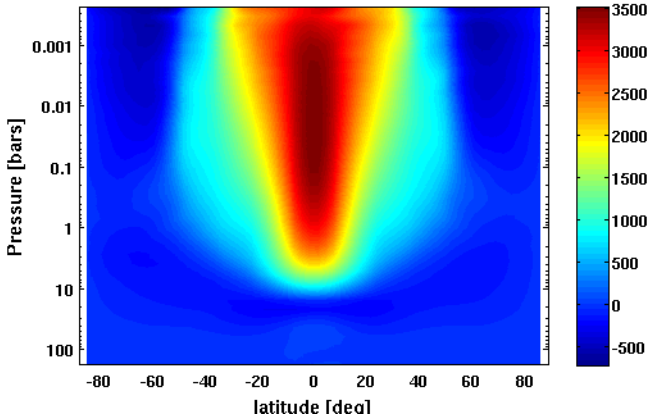

Figure 5. Zonal-mean zonal winds for our nominal HD 189733b simulation at solar abundance. This is the same simulation as in Figure 4. Scale bar gives speeds in m s^{-1}.

(A color version of this figure is available in the online journal.)

On average, the dayside is hotter than the nightside, but the dynamics distorts the temperature pattern in a complex manner (Figure 4). Perhaps most importantly, the hottest regions do not occur at the substellar longitude; instead, advection associated with the equatorial jet shifts the hottest regions downwind (eastward) of the substellar point by ∼50°. This point has been previously emphasized by Showman & Guillot (2002); Cooper & Showman (2005), and Showman et al. (2008a). Moreover, the coldest regions do not occur at the equator but instead within two broad gyres centered at latitudes of ±40°–50° and longitudes ∼60°–80° east of the antistellar point—a phenomenon not seen in our previous simulations with simplified forcing (Showman et al. 2008a). The horizontal wind speed is almost zero near the center of these gyres, so air parcels trapped there have long residence times on the nightside. This allows them to experience a large temperature drop due to radiative cooling. In contrast, air within the equatorial jet has only a short residence time (typically ∼1 day) on the nightside because of the fast jet speeds, leading to only modest temperature decreases via radiative cooling. Interestingly, the temperature structure shows substantial longitudinal variability even at pressures as great as 1 bar.

As compared to our previous simulations with simplified forcing (Showman et al. 2008a), our current HD 189733b simulations exhibit modest lateral temperature contrasts. The horizontal temperature differences reach ∼450 K at 1 bar and ∼750 K at 1 mbar (Figure 4). In contrast, in our previous simulations forced by Newtonian heating/cooling (Showman et al. 2008a), the day–night temperature differences reached nearly 900 K at 100 mbar and 1000 K at 10 mbar. The smaller values in our present simulations, which can be attributed to our usage of realistic radiative transfer, have major implications for light curves and spectra (Section 3.2).

Note that the global-scale temperature structure exhibits significant vertical coherency throughout the observable atmosphere (Figure 4). Although the detailed structure varies between levels, the hottest regions lie east of the substellar point throughout, with the longitudinal offset of the hottest region varying only modestly between pressures of 1 bar and 1 mbar. Likewise, the locations (though not the shape) of the coldest regions also maintain coherency across this pressure range (blue regions in Figure 4). At first glance, this vertical coherency is surprising, because idealized radiative calculations have shown that the radiative time constant should vary by orders of magnitude over this pressure range (Iro et al. 2005; Fortney et al. 2008; Showman et al. 2008a). At pressures where the radiative time constant is comparable to the time for wind to advect across a hemisphere, one expects a significant offset of the hottest regions from the substellar point (Showman & Guillot 2002). However, at low pressures where the expected radiative time constants are much shorter than plausible advection times, one expects the temperature patterns to track the stellar heating, with the hottest region occurring close to the substellar point (Cooper & Showman 2005; Knutson et al. 2007). Indeed, precisely this height-dependent pattern is seen in published three-dimensional simulations that force the flow with a simplified Newtonian heating/cooling scheme, which relaxes the temperature toward the radiative-equilibrium temperature profile over the expected radiative timescale (Showman et al. 2008a; Fortney et al. 2006a; Cooper & Showman 2005, 2006).

So what causes the vertical coherency in our current simulations? The simple arguments described above—in which the temperature approaches radiative equilibrium if radiation times are less than advection times—implicitly assume that the radiative-equilibrium temperature profile can be independently defined and that it has a structure reflecting that of the insolation, with the greatest radiative-equilibrium temperature at the substellar point. However, this argument neglects the fact that, in real radiative transfer, the *radiative-equilibrium temperature profile itself* depends on the dynamical response and can involve radiative interactions between different levels.[10] To illustrate, suppose the small heating rates at ∼1 bar lead to a hot region shifted east of the substellar point (as seen in Figure 4, bottom panel). Upwelling infrared radiation from these hot, deep regions will warm the entire overlying atmosphere, leading to a temperature pattern at low pressure that has similar spatial structure as that at higher pressure. These effects were ignored in our previous studies adopting Newtonian cooling (Showman et al. 2008a; Fortney et al. 2006a; Cooper & Showman 2005, 2006), but they are self-consistently included here and can explain the vertical coherency in Figure 4 despite the large expected vertical variations in radiative time constant. Nevertheless, our 5 and 10-times-solar HD 189733b simulations (and especially the HD 209458b simulations with TiO and VO opacity to be discussed in Section 5) exhibit less vertical coherency than shown in Figure 4.

Despite these quantitative differences, our current simulations lie within the same basic dynamical regime as our previous three-dimensional simulations driven by Newtonian cooling (Showman et al. 2008a; Cooper & Showman 2005, 2006). In all these cases, the flow exhibits a broad, eastward equatorial jet with westward flow at high latitudes; eastward displacements of the hottest regions from the substellar point (at least over some range of pressures); and a gradual transition from a banded flow at depth to a less-banded flow aloft. Moreover, in all these cases, the flow structures have horizontal lengthscales comparable to the planetary radius, consistent with the large Rhines scale and Rossby deformation radius for these planets (Showman & Guillot 2002; Menou et al. 2003; Showman et al. 2008b).

Figure 6 (top panel) illustrates the diversity of vertical temperature profiles that occur. Red (blue) profiles lie equatorward (poleward) of 30° latitude. This is for our nominal HD 189733b

[10] A more rigorous way of stating this is that one cannot define a radiative equilibrium temperature structure in isolation from the dynamics. In that case, the comparison-of-timescales argument fails and one must solve the full radiative-dynamical problem, as we are doing here.

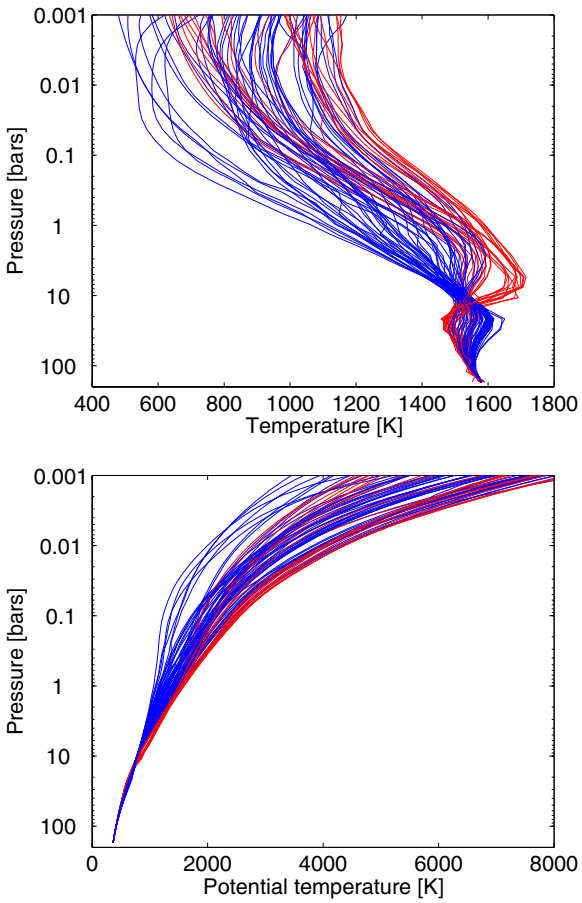

Figure 6. Selection of profiles of temperature (top) and potential temperature (bottom) vs. pressure in our nominal, solar-abundance HD 189733b simulation (the same simulation as in Figure 4). Red (blue) profiles are equatorward (poleward) of 30° latitude.

(A color version of this figure is available in the online journal.)

simulation with solar abundance; qualitatively similar patterns occur for 5 and 10 times solar. Key points are as follows. First, as expected, equatorial regions are on average warmer than the high latitudes at pressures less than a few bars. At low pressures, longitudinal variation is comparable to the latitudinal variation. Second, the temperature declines smoothly with altitude from ∼3 bars to ∼10 mbar. This has important implications for spectra and light curves, which originate within this layer. Third, dynamics has modified the deep stable radiative layer from 10 to 100 bars, leading to significant latitude variation of both temperature and static stability, with warm poles and a cold equator.

Our HD 189733b simulations remain convectively stable everywhere throughout the atmosphere. This is illustrated in Figure 6 (bottom panel), which shows the potential temperature θ versus pressure for the same profiles depicted in the top panel. Potential temperature is a measure of entropy; an atmosphere that is neutrally stable to convection has θ constant with height, whereas θ increases with altitude in a statically stable atmosphere (e.g., Salby 1996, pp. 166–172). As can be seen in Figure 6 (bottom panel), θ increases with altitude in all the profiles. This is true even on the nightside. Nightside cooling (which tends to be stronger at low pressure than high pressure) reduces the static stability of the nightside profiles relative to the dayside profiles, but in our simulations this effect is insufficient to generate a detached convection layer on the nightside.

Simulations of HD 189733b performed using opacities corresponding to 5- and 10-times-solar abundances exhibit similar behavior to our solar case depicted in Figures 4–6. The primary difference is that, compared to the solar case, the 5- and 10-times-solar cases have slightly warmer daysides, slightly cooler nightsides, and smaller eastward offsets of the hot region from the substellar point, especially at low pressure. At 1 bar, in all three cases, the approximate centroid of the hottest regions lie ∼80° east of the substellar point. At 1 mbar, however, the offset drops to ∼50° in the solar case but only ∼20° in the 5- and 10-times-solar cases. These differences can be attributed to the greater opacities in the 5 and 10-times-solar cases, which lead to greater heating rates and hence shorter radiative time constants. Despite the differences, we emphasize that all three cases exhibit extremely similar *qualitative* temperature and wind patterns.

3.2. Spectra and Light Curves

We now turn to spectra and light curves. Because our simulations couple dynamics to radiative transfer, our model output includes the emergent spectral flux versus wavelength everywhere on the model grid at each timestep. However, because we use a relatively small number ($N_\lambda = 30$) of correlated-k wavelength bins, any spectra calculated from this output would have coarse spectral resolution. Thus, we instead recalculated the emergent fluxes offline at greater spectral resolution ($N_\lambda = 196$). To do so, we took the three-dimensional temperature output at a given time and ran each vertical $T(p)$ column through our one-dimensional spectral solver to calculate upward and downward fluxes versus wavelength, taking care to use the same opacity database and stellar model as used in the original three-dimensional simulation. The resulting emergent fluxes are essentially identical to those generated by the three-dimensional model except that they have higher spectral resolution. We then calculate disk-integrated spectra and light curves using the procedures described in Showman et al. (2008a) and Fortney et al. (2006a). Planetary limb darkening (or brightening), as viewed by the observer, is accounted for.

Figure 7 shows the resulting spectra for our solar-abundance HD 189733b simulation at six orbital phases. Because the simulated temperatures decrease with altitude in the relevant pressure range (∼0.01–1 bar), spectral features are seen in absorption (rather than emission) throughout the orbit. Near the time of transit (black curve), the nightside faces Earth, with its cool temperatures and large vertical temperature gradients (Figure 6). This leads to relatively low fluxes with deep absorption bands of H_2O and CH_4. The hotter dayside (solid dark blue curve) has a smaller temperature gradient, leading to greater fluxes and shallower absorption bands. Interestingly, the fluxes 60° of phase before transit (magenta) are smaller than those occurring at transit, while the fluxes 60° of phase before secondary eclipse (green) exceed those occurring immediately before/after the secondary eclipse itself. This phase offset results directly from the fact that the hottest and coldest regions are shifted eastward from the substellar and antistellar points, respectively (see Figure 4).

Figure 8 shows light curves calculated in *Spitzer* bandpasses for our HD 189733b simulations with opacities corresponding to solar (top panel) and five-times-solar (bottom panel) abundances, respectively. Black, red, green, dark blue, light blue, and magenta show the simulated light curves at 3.6, 4.5, 5.8, 8, 16, and 24 μm, respectively. Overlaid are the Knutson et al. (2007) 8 μm light curve in small blue dots and the binned Knutson

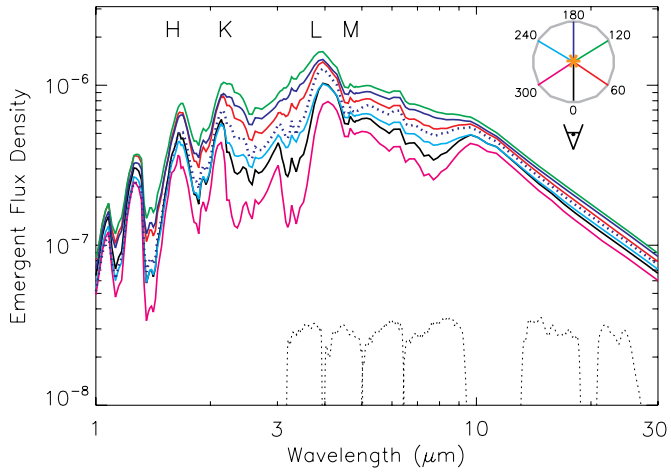

Figure 7. Emergent flux density (ergs^{-1}cm^{-2}Hz^{-1}) from our nominal, solar-abundance simulation of HD 189733b at six orbital phases. Black, nightside, as seen during transit; red, 60° after transit; green, 120° after transit; dark blue, dayside, as seen during secondary eclipse; light blue, 60° after secondary eclipse; and magenta, 120° after secondary eclipse. The key in the top right corner is color-coded with the spectra to illustrate the sequence. Thin dotted black lines at the bottom of the figure show normalized *Spitzer* bandpasses and the letters at the top show locations of the *H*, *K*, *L*, and *M* bands. This is the same simulation as in Figure 4. For comparison, the dotted curve is a spectrum from a one-dimensional planetwide average radiative-equilibrium model.

(A color version of this figure is available in the online journal.)

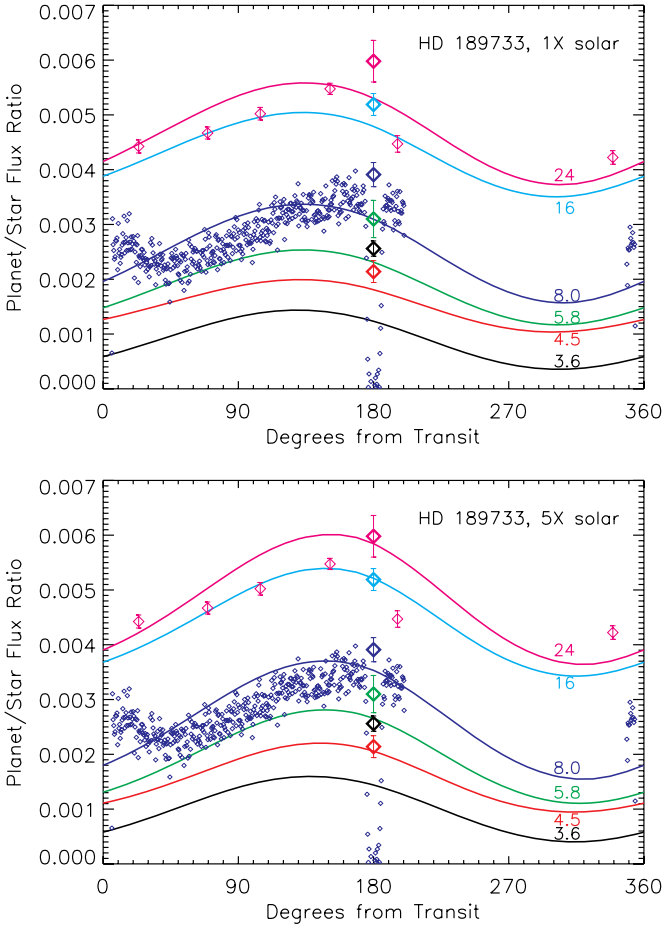

Figure 8. Light curves vs. orbital phase calculated in *Spitzer* bandpasses for HD 189733b. Top and bottom panels show light curves for our simulations using solar and five-times-solar abundances in the opacities, respectively. Within each panel, moving from bottom to top, the light curves are for wavelengths 3.6 μm (black), 4.5 μm (red), 5.8 μm (green), 8 μm (dark blue), 16 μm (light blue), and 24 μm (magenta), respectively. Overplotted is the *Spitzer* 8 μm light curve from Knutson et al. (2007) in dark blue points and the binned 24 μm light curve from Knutson et al. (2009) in small magenta diamonds. *Spitzer* secondary-eclipse depths from Charbonneau et al. (2008) and Deming et al. (2006) are plotted at 180° phase in large diamonds, with wavelengths color-coded as described above. Both simulations have a resolution of C32 with 40 layers (top panel is same simulation as in Figure 4).

(A color version of this figure is available in the online journal.)

et al. (2009) 24 μm light curve in small magenta diamonds, along with the *Spitzer* secondary-eclipse depths from Charbonneau et al. (2008) and Deming et al. (2006) in large diamonds.

Overall, our simulated light curves (Figure 8) compare favorably to the observed ones. We are able to reproduce the modest day–night flux variation seen in the observations at both 8 and 24 μm; this contrasts with our earlier simulations using Newtonian heating/cooling (Showman et al. 2008a), which greatly overpredicted the day–night flux variation. In our current solar-opacity simulations, the ratio of maximum-to-minimum flux (within a given *Spitzer* channel) ranges from 1.4 to 3.5 depending on wavelength, while in the five-times-solar case it ranges from 1.6 to 4.1, with the greatest flux ratios occurring at 3.6 μm and the smallest at 16 and 24 μm. Likewise, our simulated light curves reach their peak flux before the secondary eclipse, a feature shared by both the 8 and 24 μm light curves (Knutson et al. 2007, 2009). In the solar case (top panel), the offsets are close to 50°, whereas at five times solar (bottom panel), the offsets range from ∼26° at 24 μm to ∼42° at 3.6 μm. In the simulations, this phase offset results directly from the eastward displacement of the hottest and coldest regions from the substellar and antistellar points, respectively (Figure 4). This phenomenon also occurred in our previous simulations forced with Newtonian heating/cooling (Showman et al. 2008a; Cooper & Showman 2005; Showman & Guillot 2002).

We emphasize that the simulated light curves in Figure 8 are not fits to the observations; beyond choosing the metallicity, no tuning of any kind was performed. Instead, Figure 8 displays the natural interaction of radiation and dynamics as resolved by the model. Indeed, by explicitly representing both the dynamics and the radiation, our goal here is to eliminate the tunable knobs that have been used to parameterize dynamics and/or radiation in some previous studies.

Nevertheless, there exist some important discrepancies between the simulated and observed light curves. First, we do not reproduce the flux minimum that occurs ∼50° after transit in the observed 8 μm light curve. If real, this feature suggests the existence of a local cold region to the *west* of the antistellar point (Knutson et al. 2007). However, this flux minimum is absent in the *Spitzer* 24 μm light curve (Knutson et al. 2009), and analysis of these data suggest instead that the minimum flux region actually lies *east* of the antistellar point, which would be qualitatively consistent with our simulations. This hemisphere of the planet's surface is not well resolved by the existing light curves, which cover only half an orbit; more data are needed to resolve the issue of where the true flux minima lie (Knutson et al. 2009).

Second, the phase offsets in our simulations are somewhat too large, especially in our solar-opacity case. The observed offsets of the flux peak are 16° ± 6° at 8 μm and 20°–30° at 24 μm. In contrast, in the solar abundance simulation (top panel), the phase offsets are close to 50° at all *Spitzer* bandpasses. The agreement is better in five-times-solar case, where the simulated offsets are 30° at 8 μm and only 26°—perfectly consistent with the observed offset—at 24 μm. On the other hand, at 24 μm, the

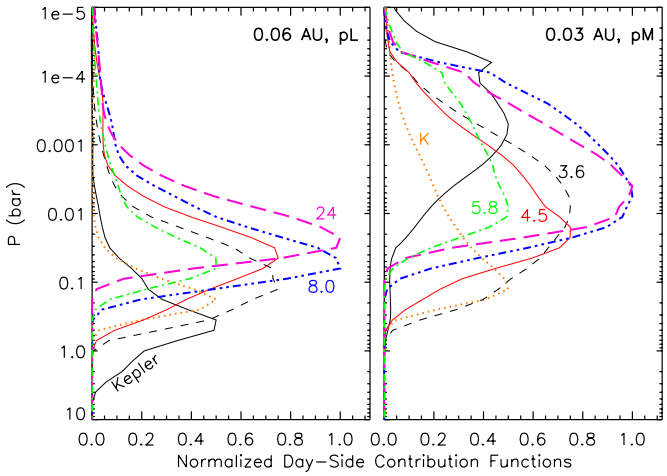

Figure 9. Contribution functions (e.g., Chamberlain & Hunten 1987; Knutson et al. 2009) calculated using our one-dimensional radiative transfer model for a generic cloud-free pL-class planet without atmospheric TiO and VO (left) and a generic pM-class planet with atmospheric TiO and VO (right). Both are for dayside conditions, and both assume solar metallicity with equilibrium chemistry. Contribution functions are calculated for various *Spitzer* broadband filters (black short dashed, red solid, green dashed-dotted, blue dashed-triple-dotted, and pink long-dashed curves for 3.6, 4.5, 5.8, 8, and 24 μm, respectively), *K* band (orange dotted curve), and the *Kepler* band at 450–900 nm (black solid curve). For clarity some of the curves have been normalized to 0.5 or 0.75 rather than 1.

(A color version of this figure is available in the online journal.)

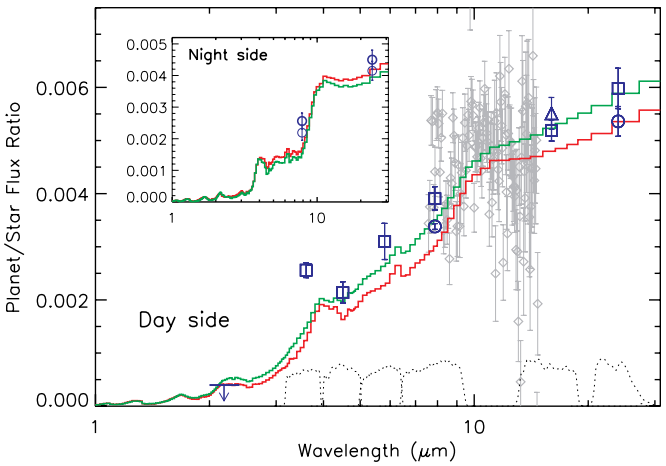

Figure 10. Planet-to-star flux ratios for our HD 189733b simulations at the time immediately before/after secondary eclipse. Red and green depict our solar and five-times-solar cases, respectively. Triangle shows the 16 μm IRS point from Deming et al. (2006). Blue squares show data from Charbonneau et al. (2008), including their re-analysis of the Deming et al. (2006) data at 16 μm. Circles at 8 and 24 μm give secondary-eclipse depths obtained from the light curves of Knutson et al. (2007, 2009). Line at 2.2 μm (*K* band) gives the upper limit from Barnes et al. (2007). Gray points give the *Spitzer* IRS spectrum from Grillmair et al. (2007). *Inset*: planet-to-star flux ratios on the nightside for these same models. Thin blue circles show the nightside flux ratios at 8 and 24 μm as obtained from the light curves of Knutson et al. (2007, 2009). Thick blue circles are those same data corrected for the effect of starspots.

(A color version of this figure is available in the online journal.)

solar case provides an overall better match to the *magnitudes* of the light curve flux values.

We now turn to the secondary-eclipse observations (large diamonds in Figure 8). We match reasonably well the eclipse depths at 4.5, 5.8, 8, 16, and 24 μm, especially with our five-times-solar-metallicity model, although it would appear that our solar model is slightly too cool. The greatest discrepancy in both models is that we underpredict the 3.6 μm secondary-eclipse depth, by factors of 2.1 and 1.8 in our solar and five-times-solar cases, respectively. Our radiative-transfer calculations suggest that 3.6 μm samples pressures of ~0.1–1 bar, deeper than any other *Spitzer* bandpass (see contribution functions in Figure 9, left panel). One possibility is that our model is too opaque at this bandpass; a lower opacity would allow photons to escape from greater pressures, where temperatures are hotter (Figure 6). Fits to the spectra of T dwarfs with the same atmospheric chemistry and radiative transfer and similar effective temperatures also suggest too much model opacity in this IRAC bandpass (Geballe et al. 2009). Alternatively, our model could simply be too cold in the 0.1–1 bar region, at least on the dayside. Interestingly, published one-dimensional models of HD 189733b also have difficulty matching the 3.6 μm point (Barman 2008; Knutson et al. 2009). A full light curve at 3.6 μm, possible with warm *Spitzer*, would be invaluable in constraining this deep layer of the atmosphere.

Figure 10 reiterates these points by displaying the planet-to-star flux ratio versus wavelength. Our solar and five-times-solar cases are depicted in red and green, respectively. Photometric data are shown in blue. The reasonable agreement at 4.5, 5.8, 8, 16, and 24 μm is evident, as is the discrepancy at 3.6 μm. Interestingly, this discrepancy is worse in our model than in published one-dimensional calculations. On the other hand, unlike current one-dimensional dayside models (Barman 2008; Knutson et al. 2009), we are able to satisfy the upper limit at 2.2 μm from Barnes et al. (2007). On the nightside (see the inset), we fare reasonably well against the 8 μm and 24 μm planet-to-star flux ratios from the light curves (blue circles).

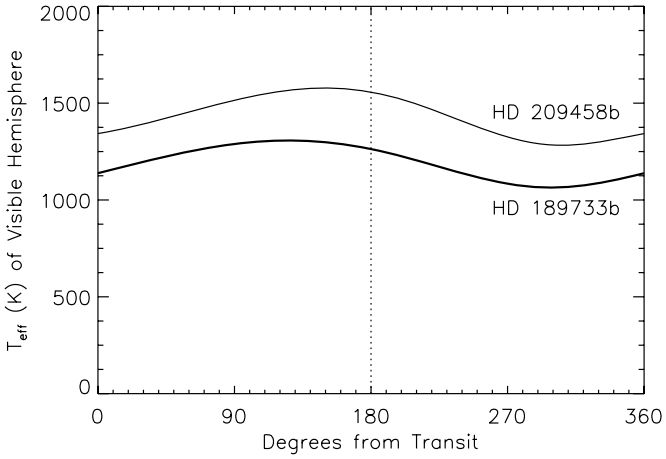

Figure 11. Effective temperature vs. orbital phase for the Earth-facing hemisphere of our nominal solar-opacity simulations of HD 189733b (thick curve) and HD 209458b (thin curve).

Figure 11 shows the total luminosity versus orbital phase for our solar-opacity simulation of HD 189733b expressed as an effective temperature. This was calculated by integrating the planet's spectrum (Figure 7) over all wavelengths to obtain a flux, dividing by the Stefan–Boltzmann constant, and taking the fourth root to obtain a temperature. The effective temperature reaches minima and maxima of ~1050 and 1250 K, respectively, and the phase offset is ~57°. As can be seen in Figure 7, much of this escaping radiation lies in the 3–5 μm range.

Our basic results are insensitive to the model resolution and integration time, as illustrated in Figure 12. The top panel shows light curves at *Spitzer* bandpasses for solar-metallicity HD 189733b simulations performed at horizontal resolutions

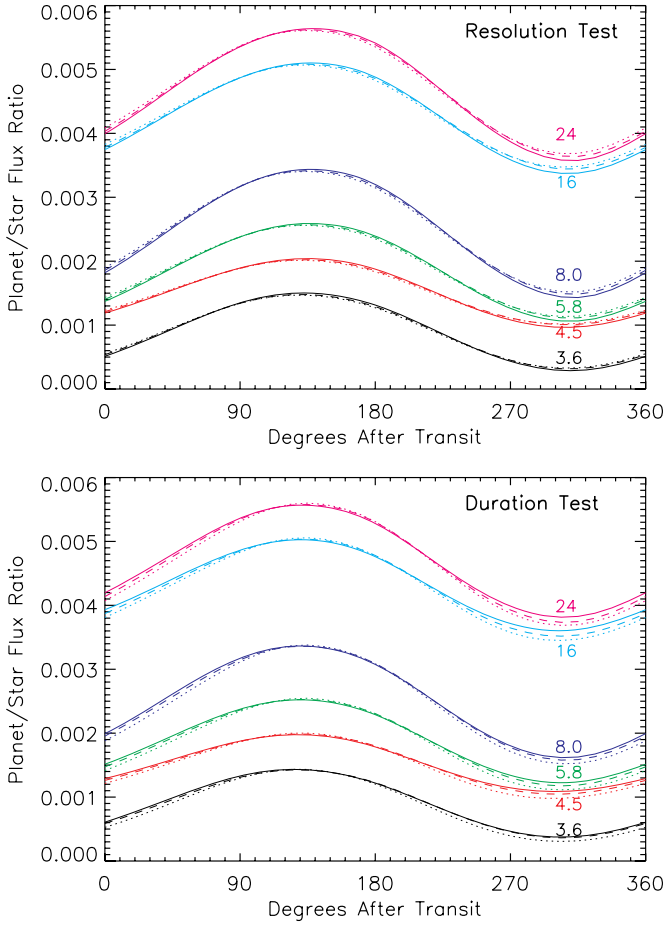

Figure 12. Sensitivity of light curves, calculated in *Spitzer* bandpasses, to model resolution (top) and integration time (bottom). Top panel shows HD 189733b simulations at horizontal resolutions of C64 (solid), C32 (dashed), and C16 (dotted), all at 301 Earth days of integration time. Bottom panel shows HD 189733b C16 simulations at 104 (dotted), 995 (dashed), and 3968 (solid) Earth days. All simulations adopt solar abundances for the opacities. Color scheme is as in Figure 8.

(A color version of this figure is available in the online journal.)

of C64 (solid), C32 (dashed), and C16 (dotted) (approximately equivalent to global resolutions of 256 × 128, 128 × 64, and 64 × 32 in longitude and latitude, respectively). All are at an integration time of 301 Earth days and have 40 vertical layers. In the bottom panel are light curves from the low-horizontal-resolution (C16) case at integration times of 104, 995, and 3968 Earth days. The simulated light curves are very similar in all these cases. This indicates that our model resolutions and integration times are sufficient to capture the dynamics.

Our simulations are consistent with recent upper limits on the temporal variability of HD 189733b reported by Agol et al. (2009). They analyzed five *Spitzer* IRAC 8 μm secondary-eclipse observations scattered over ∼370 Earth days and found that the variability in secondary-eclipse depth is less than 10% around their best-fit mean value of 0.00347. To compare with this observation, Figure 13 shows secondary-eclipse depths in the IRAC 3.6, 4.5, and 8 μm bands versus time, calculated from our HD 189733b simulation (as in Figures 8 and 12) by properly integrating the simulated infrared spectra over the *Spitzer* bandpasses. Over a period of several hundred days, our simulated variability is ∼1% at 4.5 and 8 μm and ∼1.5% at 3.6 μm, fully consistent with the Agol et al. (2009) upper limit. Interestingly, much of the predicted variability involves

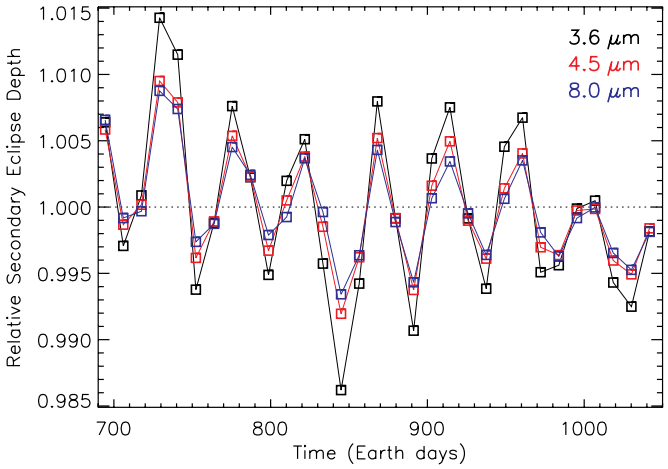

Figure 13. Secondary-eclipse depths vs. time calculated from our synchronously rotating HD 189733b simulation with solar opacity. Curves show results at the 3.6, 4.5, and 8 μm *Spitzer* IRAC bands in black, red, and blue, respectively, each normalized to its mean. Our predicted variability is ∼1%–2%, consistent with the observational 8 μm upper limit from Agol et al. (2009).

(A color version of this figure is available in the online journal.)

a coherent oscillation with a period of approximately 43 days, although a weak downward trend (corresponding to a mean decrease in eclipse depth of about 0.5%) is also present. The predominance of a single oscillation period suggests the presence of a global sloshing mode with a period of weeks; future work will be required to investigate this phenomenon and the extent to which it may depend on parameters such as the atmospheric vertical structure.

4. NONSYNCHRONOUSLY ROTATING HD 189733B

Several authors have suggested that hot Jupiters in near-circular orbits will synchronously rotate because their expected spin-down times are $\sim 10^6$ years for a Jupiter-like tidal Q of 10^5 (Guillot et al. 1996; Lubow et al. 1997). While this is plausible, no observations currently exist to constrain the rotation period of any hot Jupiter. Moreover, Showman & Guillot (2002) argued that dynamical torques between the atmosphere and interior could lead to equilibrium rotation rates that deviate modestly from synchronous. Therefore, we ran several simulations of HD 189733b to investigate the role that nonsynchronous rotation has on the dynamics and resulting observables.

Figure 14 shows the zonal-mean zonal winds versus latitude and pressure for cases with rotation rates Ω that are half, 1.5, and twice the synchronous values (top, middle, and bottom panels, respectively). These cases all assume solar metallicity and can be directly compared to their synchronously rotating counterpart in Figure 5. As can be seen, the rotation rate has a significant effect on the mean jet structure. The slowly rotating case (top) qualitatively resembles the synchronous case, with an eastward equatorial jet and westward high-latitude flows, except that the equatorial jet is narrower and faster. At rotation rates faster than synchronous, however, the equatorial jet weakens and strong eastward *polar* jets develop—a phenomena unseen in our synchronous cases. At rotation rates that are double the synchronous value (bottom), the mean speed of the polar jets exceeds that of the equatorial jet. Interestingly, these faster rotation rates are also accompanied by a general slowdown in the wind speeds; at double the synchronous rotation rate, the peak zonal-mean zonal wind speed is ∼1.6 km s^{-1}, half the value in the synchronous case.

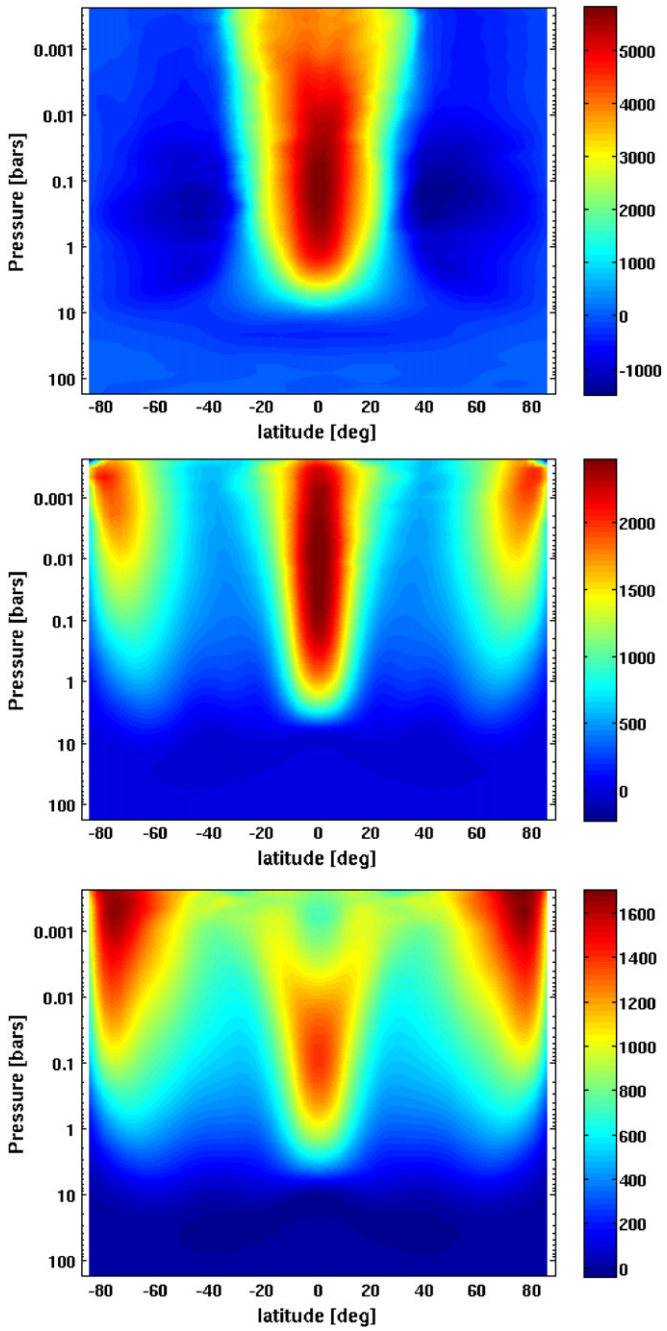

Figure 14. Effect of nonsynchronous rotation on jet structure. Shows zonal-mean zonal wind vs. latitude and pressure for HD 189733b cases with half (top), 1.5 times (middle), and twice (bottom) the synchronous rotation rate. Opacities use solar abundances. Scale bar gives speeds in $\mathrm{m\,s^{-1}}$. All simulations have a horizontal resolution of C32 with 40 layers and can be directly compared with Figure 5.

(A color version of this figure is available in the online journal.)

Two effects can influence the jet structure in these nonsynchronous cases. First, in the nonsynchronous cases, the illumination sweeps in longitude as seen in the planet's rotating reference frame—in contrast to the synchronous case, where the illuminated region is locked to a specific range of longitudes. In all cases (synchronous or not), the jets are presumably accelerated by large-scale eddies generated by the day–night heating gradient. This must particularly be true of the superrotating equatorial jet, which corresponds to a local maximum of angular momentum per mass and can only be formed by up-gradient momentum transport by eddies. Sweeping the heating pattern in longitude can potentially change the character of these jet-driving eddies and hence alter the resulting jet structure. This may explain, for example, the trend of decreasing jet speed with increasing rotation rate (Figure 14). Interestingly, the peak equatorial jet speed in an inertial reference frame—namely, the sum of the peak jet speed in Figure 14 and the planetary rotation rate of Ωa at the equator—is nearly constant (to within $\sim$15%) in all the cases shown in Figures 5 and 14.

Second, changing the rotation rate changes the strength of the Coriolis force and, particularly, the strength of the so-called "β effect," where $\beta = 2\Omega\cos\phi/a$ is the northward gradient of the Coriolis parameter. For flows driven primarily by creation of turbulence at small scales, turbulence theory predicts that jet widths in latitude scale as $\sim\pi(U/\beta)^{1/2}$, where U is a mean wind speed (Rhines 1975; Vasavada & Showman 2005). This "Rhines" scaling suggests that slower (faster) rotation rates would lead to wider (narrower) jets. In simulations of *synchronously rotating* hot Jupiters, Showman et al. (2008a) showed that faster rotation indeed leads to narrower jets and vice versa—but the dependence of jet width on rotation rate is weaker than the inverse-square-root Rhines prediction. Presumably, this deviation occurs because, in the hot Jupiter case, the jets are driven not at small scales but by eddies induced by the day–night heating gradient, which have length scales comparable to the jet widths. The differences between our nonsynchronous cases (Figure 14) and the synchronous Ω parameter variations in Showman et al. (2008a) suggest that the trends in Figure 14 cannot be explained solely by the β effect but also depend on changes in the eddy behavior as discussed above. We defer a detailed diagnosis of the dynamics of this process to a future study.

Figure 15 demonstrates that nonsynchronous rotation has a significant effect on the light curves. Interestingly, the phase offsets are smaller for the slowly rotating case (Ω half the synchronous value; top panel) and larger for the rapidly rotating cases (Ω 1.5 and two times the synchronous value; bottom panel). This behavior makes sense physically. As viewed in the synchronously rotating reference frame, the nonsynchronous rotation is equivalent to a westward motion of the planetary interior in slowly rotating case but an eastward motion of the planetary interior in the rapidly rotating cases. This rotation combines with the winds shown in Figure 14[11] to produce (as seen in the synchronous frame) a strong, latitude-averaged eastward flow in the rapidly rotating cases; in contrast, in the slowly rotating cases, the mid-latitudes flow strongly westward, although the equatorial jet is still eastward. The upshot is that the hottest regions are shifted eastward from the substellar point by a greater distance in the rapidly rotating cases than in the slowly rotating case. This leads to a small phase shift in the slowly rotating case and a large phase shift in the rapidly rotating cases (Figure 15).

Interestingly, the *shape* of the light curve is also affected—the flux peak is narrower in the slowly rotating case than in the rapidly rotating case. This seems to occur because the dayside hot regions span a smaller range of longitudes in the slowly rotating case than in the rapidly rotating cases.

[11] The winds shown in Figure 14 are those in the planet's *nonsynchronous* reference frame; to represent the winds in the *synchronously* rotating reference frame, one must add $(\Omega - \Omega_{\rm syn})a\cos\phi$, where Ω is the actual rotation rate, $\Omega_{\rm syn}$ is the rotation rate of the synchronous reference frame, a is the planetary radius, and ϕ is the latitude.

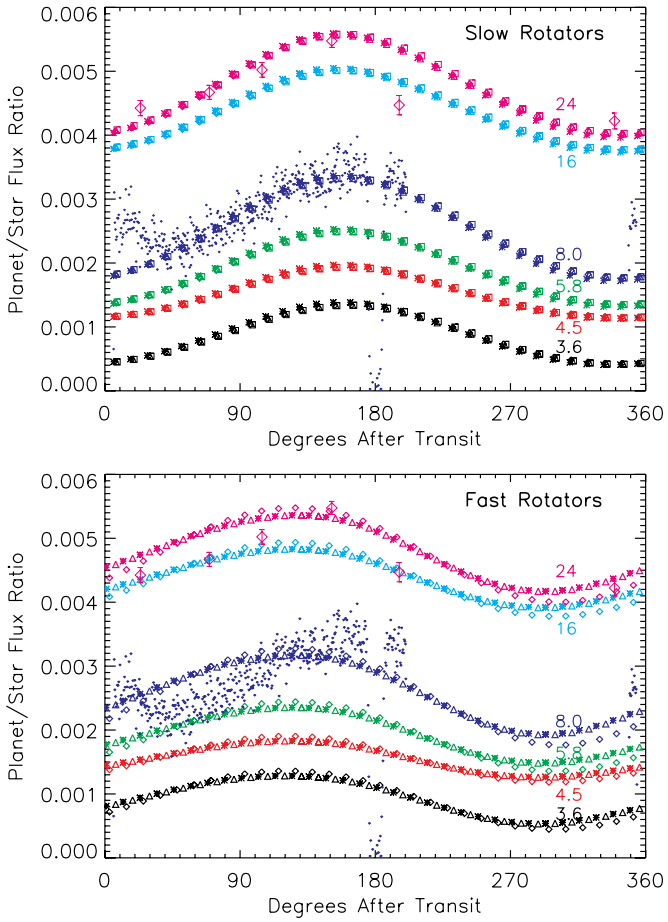

Figure 15. Light curves for our nonsynchronous, solar-metallicity HD 189733b simulations shown in Figure 14. Top panel shows case with half the synchronous rotation rate (squares, asterisks, and triangles denote different times). Bottom panel shows cases with 1.5 times the synchronous rotation rate (triangles and asterisks denoting different times) and twice the synchronous rotation rate (diamonds).

(A color version of this figure is available in the online journal.)

The theoretical 8 μm light curve in the slowly rotating case actually provides quite a good match to the observed 8 μm light curve, reproducing both the shape and phase offset of the flux peak. Nevertheless, we still do not reproduce the flux minimum seen after transit. The rapidly rotating cases provide a significantly poorer match at 8 μm, with a flux peak that is too broad and a phase shift that is too large. The situation is more ambiguous at 24 μm; both cases provide reasonable though not perfect matches to the observed light curve. We re-emphasize that these are not fits to data but rather are theoretical predictions. Moreover, although it could be tempting to infer a planetary rotation rate from these comparisons, this is premature, as other factors not explored here (e.g., disequilibrium chemistry) could also have large effects on the light curves.

5. SYNCHRONOUSLY ROTATING HD 209458B

5.1. Circulation Regime, Spectra, and Light Curves

Spitzer secondary-eclipse photometry shows that the 4.5 and 5.8 μm brightness temperatures of HD 209458b reach 1700–1900 K (Knutson et al. 2008). These values significantly exceed both the planet's effective temperature and the inferred brightness temperatures at the 3.6, 8, and 24 μm bands, which are closer to ~1500 K. Given these facts, Knutson et al. (2008) and Burrows et al. (2007, 2008) suggested that the atmosphere of HD 209458b contains a thermal inversion (hot stratosphere) on the dayside, with temperatures reaching ~2000 K or more.

Long before these *Spitzer* data were available, Hubeny et al. (2003) and Fortney et al. (2006b) showed that such inversions result naturally from gaseous TiO and VO, which are extremely opaque in the visible wavelength range and cause absorption of starlight at substantially lower pressures (~mbar) than would occur in the absence of these species. Undetermined photochemical products are another possible absorber (Burrows et al. 2007, 2008). Zahnle et al. (2009), for example, have suggested that disequilibrium sulfur species produced from photochemical destruction of H_2S could provide sufficient short-wavelength absorption to account for the stratospheres.

However, to date, radiative-equilibrium models of HD 209458b have been unable to reproduce the observed *Spitzer* photometry (Fortney et al. 2008): while they successfully reproduce the high 4.5 and 5.8 μm fluxes, they overpredict the 3.6, 8, and 24 μm fluxes. This suggests that the stratosphere predicted in these radiative-equilibrium models is too hot and/or too broad in vertical extent. Burrows et al. (2007) obtained better agreement, especially at 3.6 μm, by including an ad hoc heat sink to mimic the effect of day-to-night heat transport by the atmospheric circulation. By confining this sink to pressures between 0.01 and 0.1 bars, Burrows et al. (2007) were able to reproduce the low 3.6 μm flux while keeping the 4.5 and 5.8 μm fluxes high. However, as Showman et al. (2008a) pointed out, day–night heat transport is unlikely to be confined to a narrow pressure range; in the Showman et al. (2008a) three-dimensional circulation models, for example, the dayside "heat sink" (expressed in K s^{-1}) caused by dynamics increases monotonically with decreasing pressure from ~10 bars to the top of their model at 0.001 bar (their Figure 10). Thus, an important question is whether a three-dimensional dynamical model, coupled to realistic radiative transfer and including TiO/VO opacity, can match the observed secondary-eclipse spectrum of HD 209458b.

Light curves are also of interest. From several brief *Spitzer* observations at different phases, Cowan et al. (2007) placed a 2σ upper limit of 0.0015 on the peak-to-peak phase variation in the planet/star flux ratio at 8 μm. This suggests that the difference in the planet's day and night 8 μm brightness temperatures is less than a few hundred K. In contrast, Fortney et al. (2008) suggested that, as a pM-class planet, HD 209458b should exhibit much greater phase variations in the mid-IR than planets lacking atmospheric TiO/VO. Physically, the idea is that the presence of TiO and VO moves the photospheres upward to low pressure, where the radiative time constants are short and the air can experience rapid dayside heating and nightside cooling. In contrast, planets without atmospheric TiO/VO would have deeper photospheres, where the radiative time constants are longer than typical advection times, thus yielding more modest day–night phase variations. Fortney et al. (2008) also suggested that phase offsets of the hottest/coldest regions from the substellar/antistellar points would be smaller for pM-class planets than for pL-class planets. We here wish to test these ideas by determining the circulation patterns and light curves for a model of HD 209458b with TiO/VO opacity. Note that even if hot-Jupiter stratospheres turn out to result from shortwave absorption by compounds other than TiO and VO (e.g., Zahnle et al. 2009), our simulations will give a qualitative picture of how dynamics responds to the presence of a compound that absorbs strongly in the visible.

Thus, we performed several simulations of HD 209458b including TiO and VO opacity in chemical equilibrium. When temperatures are too cold for TiO and VO to exist in the gas phase, they are absent, but when temperatures are warm enough, they are included.

Our HD 209458b simulations develop vigorous circulations that, as expected, include a hot dayside stratosphere. This is illustrated in Figure 16, which shows the temperature and horizontal wind patterns at pressures of 1 bar, 30 mbar, 1 mbar, and 0.1 mbar (bottom to top) for our case with solar abundances. At deep levels (1 bar and 30 mbar), the circulation qualitatively resembles that of HD 189733b, with an eastward equatorial jet, westward high-latitude flows, and a hot region shifted east of the substellar point (compare the bottom two panels of Figures 4 and 16). Nevertheless, even at these deep levels, localized regions attain temperatures sufficient for TiO/VO to exist in the gas phase (∼1700–1900 K).

By pressures of 1 mbar, the picture changes drastically: a "baby" stratosphere with a radius of 50° in longitude and latitude has developed, with temperatures reaching 2000 K (Figure 16, second panel). This stratosphere is approximately centered on the substellar point, with an eastward offset of only ∼10° longitude. Its spatial confinement results from the fact that only air within ∼50° of the substellar point receives sufficient irradiation to achieve temperatures necessary for gas-phase TiO and VO to exist. Air >60° from the substellar point, although still on the dayside, has temperatures too low for gas-phase TiO/VO, and without the benefit of the extra opacity supplied by these species, this air remains substantially cooler (<1400 K). This nonlinear feedback between temperature and opacity leads to a remarkably sharp temperature gradient, with temperatures dropping from 1800 to 1400 K as one moves from 50° to 60° angular distance from the substellar point.

At still lower pressures, an even greater fraction of the starlight is available to cause heating, and the stratosphere becomes horizontally larger until it covers most of the dayside at pressures ⩽0.1 mbar (Figure 16, top panel). Although the equatorial winds at these low pressures involve a significant eastward flow at most longitudes, the mid- and high-latitude winds involve a simpler motion that, to zeroth order, moves air away from high-temperature regions toward low-temperature regions. At low pressure, the temperature pattern is relatively symmetric about the substellar and antistellar points, as suggested observationally for Ups And b (Harrington et al. 2006) and HD 179949 (Cowan et al. 2007).

A contributing factor to the widening of the stratosphere with altitude is that stellar radiation is absorbed at lower pressure near the limb than at the substellar point, which results directly from the longer atmospheric path length to stellar irradiation at the limb ($\mu \to 0$) than at the substellar point ($\mu = 1$). Thus, near the limb the heating peaks at lower pressure, confining the stratosphere to low pressures. Near the substellar point, the heating peaks deeper, allowing the stratosphere to extend more deeply in this localized region.

Our simulated stratospheres result directly from the existence of gaseous TiO and VO on the dayside in these simulations. Simulations of HD 209458b performed *without* gaseous TiO/VO lack stratospheres and develop temperature and wind patterns resembling a hotter version of our HD 189733b simulations. Likewise, our previous HD 209458b simulations performed with Newtonian heating/cooling (Showman et al. 2008a) developed a weak dayside temperature inversion but nothing resembling the extremely hot stratosphere shown in Figure 16.

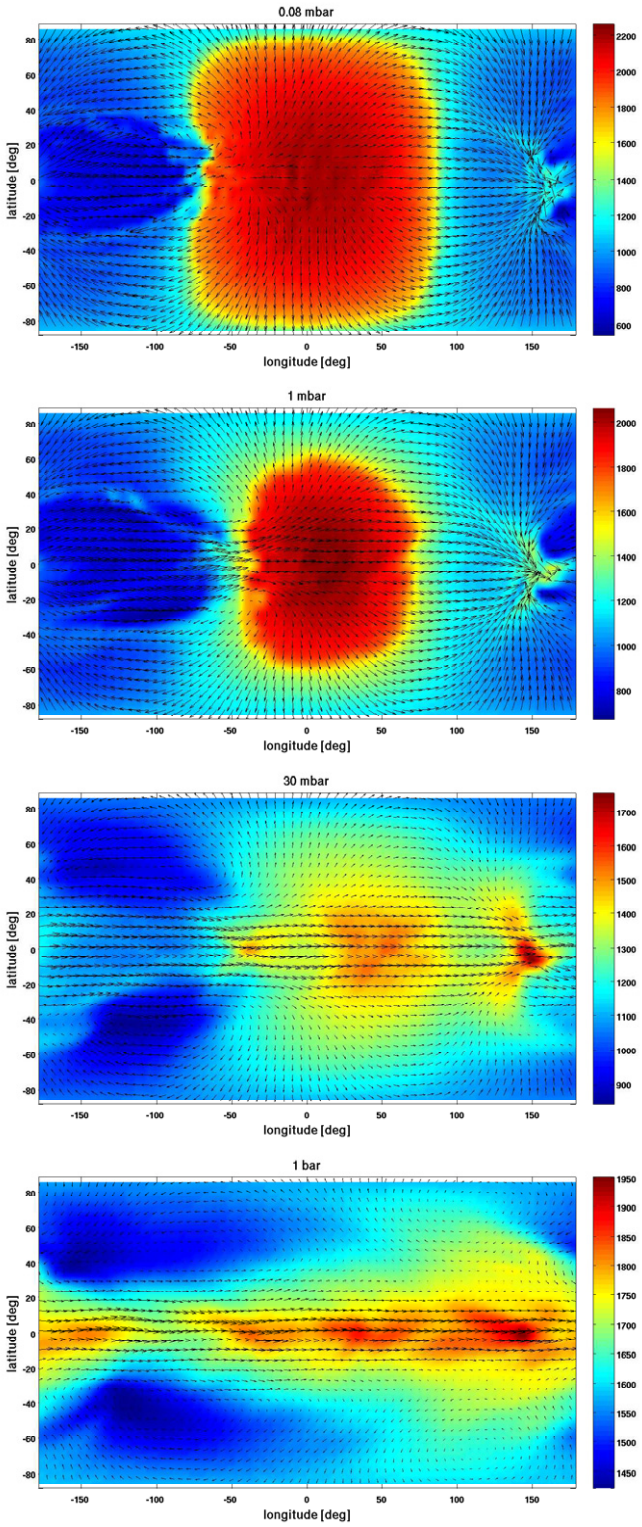

Figure 16. Temperature (colorscale, in K) and winds (arrows) for nominal HD 209458b simulation with solar abundances including TiO/VO. Panels show flow at 0.1 mbar (top), 1 mbar (second panel), 30 mbar (third panel), and 1 bar (bottom panel). Horizontal resolution is C32 (roughly equivalent to a resolution of 128 × 64 on a longitude/latitude grid) with 53 vertical layers. Substellar point is at longitude, latitude (0°, 0°). Note the development of the dayside stratosphere.

(A color version of this figure is available in the online journal.)

To illustrate the height-dependence of the composition (which affects the opacity), Figure 17 depicts the chemical-equilibrium

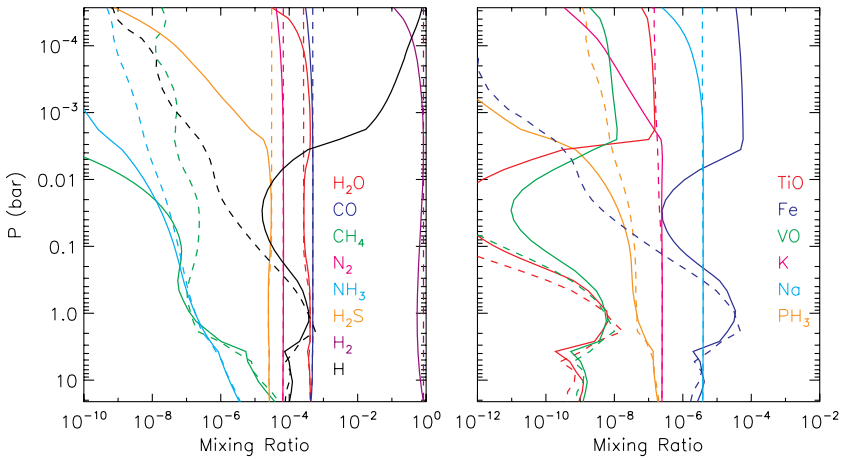

Figure 17. Chemical-equilibrium abundances of several molecules vs. pressure at the substellar point (solid) and antistellar point (dashed) from our three-dimensional HD 209458b case adopting solar abundances.

(A color version of this figure is available in the online journal.)

abundances versus pressure at the substellar point (solid) and antistellar point (dashed) for our nominal HD 209458b case. At low pressure, TiO is abundant on the dayside yet depleted on the nightside.

Importantly, our simulated stratospheres do not extend fully *to* the terminators (which are at longitudes ±90° in Figure 16). Generally, the terminators themselves have temperatures of ∼1300 K or less. The net heating there is simply too low to allow temperatures above the TiO/VO condensation curves. Thus, while much of the dayside could have abundant TiO and VO, our simulations suggest that these species will be largely absent (or at least depleted) on the limbs as seen during primary transit. This will have important implications for interpreting transit spectra of HD 209458b (e.g., Sing et al. 2008) and other pM-class planets. Interestingly, note that our simulated stratosphere approaches the terminator to the *east* of the substellar point more closely than it approaches the terminator to the *west* of the substellar point—the result of thermal advection due to the eastward equatorial jet. This result suggests that, during transit, the planet's leading limb will be cooler and more depleted in TiO/VO than the trailing limb.

The diversity of temperature–pressure profiles in our solar model is shown in Figure 18. Near the bottom is the quasi-isothermal region from ∼ 3–100 bars. Above that, from pressures of ∼1 bar to 30 mbar, the temperature decreases with altitude on both the dayside and the nightside. At pressures less than ∼10 mbar, the dayside stratosphere is evident, with temperatures exceeding 2000 K.

Figure 19 shows spectra at six orbital phases. Within ∼60° orbital phase of transit (magenta, black, and red curves), molecular bands are seen in absorption because the temperature decreases with increasing altitude on the nightside. Near secondary eclipse, however, when the dayside faces Earth, the features flip into emission (green, dark blue, and light blue curves), which results directly from the dayside temperature inversion associated with the stratosphere. This differs from our HD 189733b simulations, where molecular features are seen in absorption at all orbital phases, including the dayside (Figure 7). Nevertheless, as the effective temperature of this HD 209458b simulation makes clear (Figure 11), the dayside radiation arrives primarily from the *bottom* of the stratosphere where mean temperatures are a modest ∼1500 K (rather than from higher-altitude regions where temperatures exceed 2000 K).

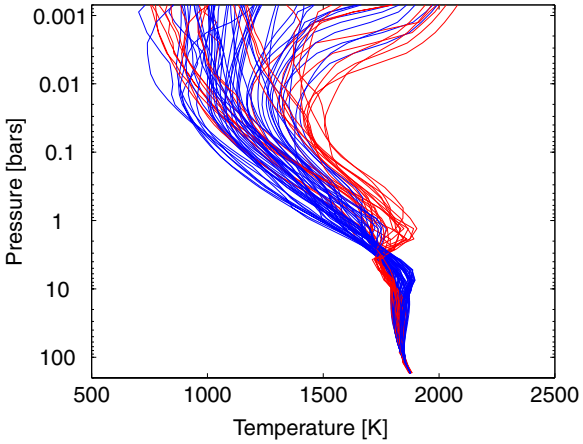

Figure 18. Selection of temperature–pressure profiles for our nominal, solar-abundance HD 209458b simulation including TiO and VO opacity (same simulation as in Figure 16). Red (blue) profiles are equatorward (poleward) of 30° latitude. Note the formation of the stratosphere at pressures less than ∼30 mbar.

(A color version of this figure is available in the online journal.)

Figure 20 compares our simulated HD 209458b dayside planet/star flux ratio spectrum to the *Spitzer* secondary-eclipse photometry of Knutson et al. (2008, 2009) and Deming et al. (2005), including a tentative revision to the 24 μm eclipse depth by Deming (personal communication). We match the secondary-eclipse depths at 3.6 and 8 μm. However, despite the existence of a stratosphere in our simulations, our solar-opacity case underpredicts the eclipse depths at 4.5 and 5.8 μm by nearly 50% (roughly 3σ and 2.3σ, respectively, at these two bands). We also miss the 24 μm eclipse depth of Deming et al. (2005) (the lower point in Figure 20) by roughly 2.5σ, although we fall within 2σ if the tentative revision to this point (upper point in Figure 20) turns out to be more appropriate.

These discrepancies suggest that our simulated stratosphere does not have the correct properties (e.g., temperature or altitude range). A comparison of our temperature profiles (Figure 18) to the radiative-equilibrium profiles of Fortney et al. (2008, their Figure 12), who match the 4.5 and 5.8 μm points but overpredict the others, shows that the hottest of our stratospheric profiles qualitatively resembles theirs. However, because our dayside

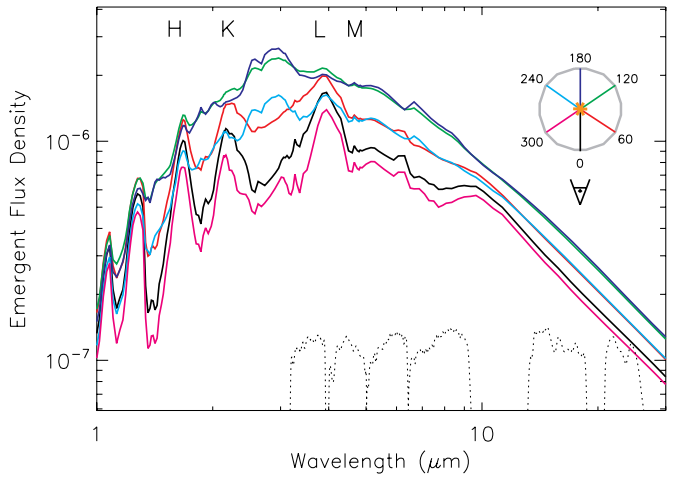

Figure 19. Emergent flux density (erg s^{-1} cm^{-2} Hz^{-1}) from our nominal, solar-abundance simulation of HD 209458b, including TiO and VO opacity, at six orbital phases. Black, nightside, as seen during transit; red, 60° after transit; green, 120° after transit; dark blue, dayside, as seen during secondary eclipse; light blue, 60° after secondary eclipse; and magenta, 120° after secondary eclipse. The key in the top right corner is color-coded with the spectra to illustrate the sequence. Thin dotted black lines at the bottom of the figure show normalized *Spitzer* bandpasses and the letters at the top show locations of the *H*, *K*, *L*, and *M* bands. This is the same simulation as in Figure 16.

(A color version of this figure is available in the online journal.)

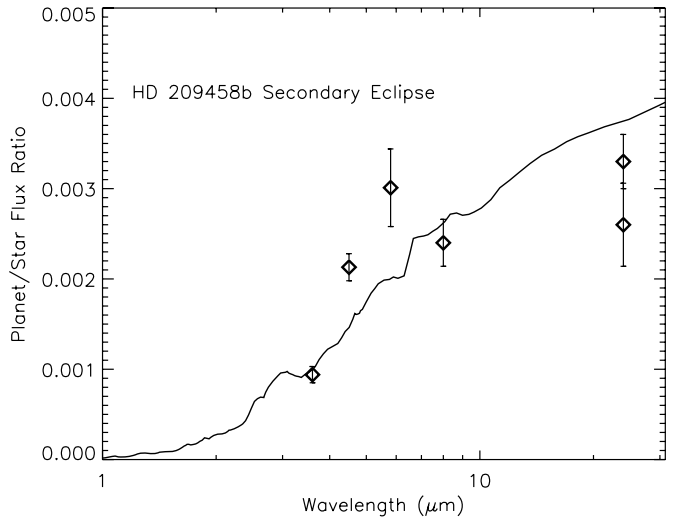

Figure 20. Planet-to-star flux ratio vs. wavelength for our HD 209458b simulation at the time immediately before/after secondary eclipse (solid curve). The simulation adopts solar abundances including TiO/VO opacity. Points show measured secondary-eclipse depths (Deming et al. 2005; Knutson et al. 2008, 2009).

includes a range of profiles ranging from hot to cold, our *dayside average* profile is colder than theirs. This may help explain the fact that our predicted dayside fluxes are systematically lower than those of Fortney et al. (2008). Presumably, this difference results from the vigorous dayside-to-nightside transport of thermal energy by the atmospheric circulation in our case.

When a spectrum exhibits greatly differing brightness temperatures at different wavelengths (as is true for HD 209458b), a common explanation is that the different wavelengths sense different pressure levels (because of the wavelength-dependent opacities). In the presence of a vertically varying temperature, this can produce a spectrum with wavelength-varying brightness temperatures.

In this context, a fundamental stumbling block to simultaneously explaining the five *Spitzer* secondary-eclipse depths is that the range of pressures that contribute photons to the 3.6, 4.5, 5.6, 8, and 24 μm bands are all very similar—at least for the radiative-transfer model, chemical composition, and opacities adopted here. Contribution functions calculated for each of these *Spitzer* bands (see Figure 9, right panel) peak between 3 and 10 mbar, and they all have very broad tails extending to ~0.1 mbar on the low-pressure side and ~100 mbars on the high-pressure side.[12] This overlap in pressure means the brightness temperatures in all these bands tend to be similar. Thus, it is difficult to produce a high brightness temperature in some bands (such as at 4.5 and 5.8 μm) while maintaining low brightness temperature in other bands (such as at 3.6, 8, and 24 μm)—as apparently required by the data. This problem is not confined to the present study; it helps explain the difficulty Fortney et al. (2008) had in explaining all the observations. Even Burrows et al. (2007), who had the flexibility of several free parameters governing an assumed stratospheric absorber and the magnitude and pressure range of the parameterized dayside heat sink, were unable to match the 5.8/8 μm flux ratio. Separating the pressure ranges of the contribution functions would require differential changes to the opacities at the wavelengths of *Spitzer* bandpasses. Potentially, alternate (i.e., disequilibrium) chemical compositions could sufficiently affect the opacities to resolve this conundrum; investigating this possibility will require future work. Disequilibrium chemistry has been invoked to explain infrared spectra of L dwarfs with similar effective temperatures (Leggett et al. 2007).

We now turn to infrared light curves. Figure 21 shows light curves in *Spitzer* bandpasses calculated for our HD 209458b case with solar abundances. As was the situation with HD 189733b, our current HD 209458b light curves exhibit muted phase variations relative to those obtained from our earlier simulations using Newtonian heating/cooling (Showman et al. 2008a; Fortney et al. 2006a). In the current simulations, the ratio of maximum-to-minimum planet/star flux ratio (at a given wavelength) is nearly 2 at all four IRAC bands and ~1.6–1.7 at the 16 μm IRS and 24 μm MIPS bands. The *difference* between maximum and minimum values increases with wavelength and is 0.0014 at 8 μm. Phase offsets range from ~20° at the longer wavelengths to almost 40° at 3.6 μm. These values are significantly nonzero but are smaller than their counterparts for our solar-abundance HD 189733b simulations (Figure 8, top panel), consistent with the general trend suggested by Fortney et al. (2008).

Our muted phase variations are consistent with the observational constraint of Cowan et al. (2007), who found a 2σ upper limit of 0.0015 on the phase variation of HD 209458b at 8 μm. Figure 21 also reiterates our agreement with the 3.6 and 8 μm secondary-eclipse photometry and our discrepancy at 4.5 and 5.8 μm. Continuous light curves over half an orbit have recently been obtained at 8 and 24 μm and are possible at 3.6 and 4.5 μm with warm *Spitzer*, which would provide a test of our models and insights on how to explain the discrepancies noted above.

The muted phase variations in Figure 21 are particularly intriguing given that we *do* have a dayside stratosphere and (as a result) enormous day–night temperature variations reaching

[12] These pressure ranges are specific to the solar model including TiO and VO. Contribution functions calculated *without* TiO/VO for HD 189733b using the same radiative-transfer code peak at substantially deeper pressures of 30–100 mbar. See Figure 9.

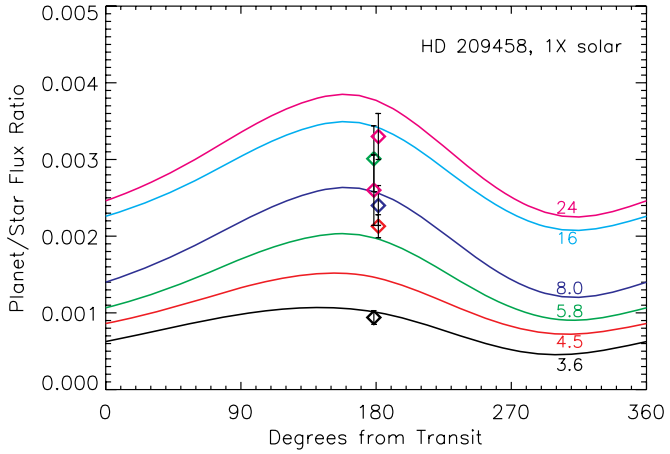

Figure 21. Light curves vs. orbital phase calculated in *Spitzer* bandpasses for our HD 209458b case with solar abundances. Within each panel, moving from bottom to top, the light curves are for wavelengths 3.6 μm (black), 4.5 μm (red), 5.8 μm (green), 8 μm (dark blue), 16 μm (light blue), and 24 μm (magenta), respectively. Overplotted are the *Spitzer* secondary-eclipse measurements from Knutson et al. (2008) in large diamonds, color-coded to the light curves.

(A color version of this figure is available in the online journal.)

$\sim$1500 K at low pressure. There are two possible reasons to reconcile why these large day–night temperature variations do not translate into large day–night flux variations. First, much of the radiation that contributes to the dayside fluxes emanates from altitudes near the bottom of the stratosphere, where day–night temperature differences are modest. This is exacerbated by the fact that the stratosphere only covers part of the dayside. Thus, a substantial fraction of the dayside flux does not emanate from the stratosphere but from deeper layers and surrounding regions that are cooler. This lowers the dayside flux compared to an idealized case where all the dayside mid-IR radiation comes from the stratosphere. Second, the cooler temperatures on the nightside means that the mid-IR photospheres on the nightside are deeper in pressure—by roughly an order-of-magnitude—than those within the dayside stratosphere. Because temperatures increase with pressure on the nightside, this elevates the nightside flux relative to an idealized case where the photospheres remain at the same (low) pressure everywhere. Both these effects act to mute the phase variations in the mid-IR, at least in the *Spitzer* bandpasses.

Note, however, that the expected IR phase variations can depend sensitively on wavelength. As can be seen in Figure 19, for example, our HD 209458b model predicts that the peak phase variations reach factors of $\sim$4 in specific wavelength bands near 1.5, 1.8, and 2.8 μm, with relatively smaller phase variations (factors of $\sim$2 or less) at intermediate wavelengths. Since both large and small day–night phase variations can occur on a single object (depending on wavelength), caution is needed when attempting to link the amplitude of phase variation to the efficiency of day–night heat transport—especially if one only possesses light curves at only one or two wavelengths. Light curves obtained in numerous isolated bands across this region (or low-to-moderate resolution spectra at different orbital phases) by a future space mission could shed considerable insight into the atmospheric composition and three-dimensional temperature structure.

5.2. Discussion

Our results point toward possible refinements of the scenario outlined in Fortney et al. (2008). They anticipated large day–night flux differences for pM-class planets, including HD 209458b. This contrasts with the modest phase variations we find here. However, the fact that we underpredict the dayside 4.5 and 5.8 μm fluxes for HD 209458b suggests that *in reality* (as opposed to in our simulations) the day–night flux variations will be large at these two wavelengths. If similar flux ratios are found for other planets with day-side temperature inversions (XO-1b may point to this; see Machalek et al. 2008), a revision to the Fortney et al. (2008) scenario may be in order, wherein HD 209458b and other transitional pM-class planets will have large phase variations at 4.5 and 5.8 μm but modest phase variations at the other *Spitzer* bandpasses. *K* band, sensing even deeper than $\sim$100 mbar, should also exhibit only modest phase variations. This scenario reconciles the secondary-eclipse spectrum of HD 209458b with the observational upper limit on the phase variation at 8 μm (Cowan et al. 2007).

But what of hotter planets? Fortney et al. (2008) positioned HD 209458b near the pL/pM boundary and acknowledged that this transition could be indistinct because of the extended temperature range over which TiO and VO condense (Lodders 2002). Planets more strongly illuminated than HD 209458b should have hotter stratospheres that cover more of the dayside, and it remains possible that such "very hot Jupiters" could indeed have large day–night phase variations in most *Spitzer* channels as predicted by Fortney et al. (2008). The strong observational evidence that ups And b (Harrington et al. 2006) and HD 179949b (Cowan et al. 2007) show large day–night flux contrast at 24 and 8 μm, respectively, may indicate such a change in temperature structure at the higher incident fluxes ($\sim$35% higher than HD209458b) that these planets receive. Although neither of these planets eclipse, Barnes et al. (2008) have suggested that HD 179949b has a dayside temperature inversion. It will be interesting to perform three-dimensional simulations of these and hotter planets, particularly ones that go through secondary eclipse. Obtaining light curves for very hot eclipsing systems, such as TrES-4 and HAT-P-7b, should be important goals for warm *Spitzer* or the *James Webb Space Telescope*.

For all of these systems, whether large day–night flux contrasts in the IR translate into large day–night effective temperature contrasts can only be unambiguously answered by light curves across many wavelengths, preferably from 2–5 μm, around the peak in planetary flux (e.g., Barman 2008). This makes 3.6 and 4.5 μm light curves from the *Spitzer* warm mission, and continued searches for planet flux in *K* band, particularly important.

Finally, we conclude this section with some discussion of the likelihood that gaseous TiO and VO can actually exist on the dayside. As discussed in Fortney et al. (2008), we calculate opacity assuming *local* chemical equilibrium at the given p and T. Assuming TiO and VO are included in the database in the first place, this means that gaseous TiO/VO opacity are included if the local temperatures are hot enough—ignoring the possibility of any "cold trap" effect that could globally deplete the abundance of these species. One possible cold trap, commonly discussed in the context of one-dimensional models, is at pressures of tens to hundreds of bars where the temperature at the bottom of the near-isothermal radiative zone is expected to be cooler than the TiO/VO condensation temperatures for multi-Gyr-old hot Jupiters farther than $\sim$0.04 AU from their stars (Hubeny et al. 2003; Fortney et al. 2008). Nevertheless, the existence of stratospheres on some planets argues that this does not occur on HD 209458b and other pM-class planets.

However, another possible cold trap—not considered by previous one-dimensional models—is the presence of the large day–night temperature difference in the observable atmosphere. As a parcel of hot dayside air flows onto the nightside, its temperature plummets and gaseous TiO and VO condense. If these Ti- and V-bearing particles settle out before the air parcel returns to the dayside, then the atmosphere could become depleted in TiO and VO even if no cold trap exists at deeper levels of tens to hundreds of bars. On the other hand, if the particles are small, their settling speeds will be slow and they will remain in the air parcel when it returns to the dayside days later. In this case, the increased temperatures will allow these particles to sublimate, resupplying gaseous TiO and VO to the atmosphere. Thus, our simulations with TiO/VO are only self-consistent if the TiO/VO particles cannot settle out on the nightside. This effectively means that the particles must remain small.

We can quantify the maximum particle sizes as follows. At 1 mbar, characteristic vertical velocities in our HD 209458b simulation are $\sim 30\,\mathrm{m\,s^{-1}}$. For particles to remain suspended, the settling velocities must be less than these values. Given the Stokes flow speed modified for gas-kinetic effects (see, e.g., Ackerman & Marley 2001, Equation (B1)), and air viscosities relevant to hydrogen at ∼1500 K, this implies particles radii less than $\sim 30\,\mu$m. At lower pressure, the gas-kinetic effects become stronger, leading to greater settling velocities; at 0.1 mbar, for example, the particles must be less than ∼7–10 μm in radius to remain suspended. (Calculation of Reynolds numbers for the falling particles shows that they are less than 1, implying that the Stokes relation is valid and that turbulent modifications to the fall velocity need not be considered.) It seems plausible that the actual particles sizes are smaller than these values, but detailed microphysical calculations will be needed to explore this further. A complicating factor is that not only TiO/VO but also silicates will condense on the nightside at low pressure.

These estimates are crudely consistent with subsequent calculations performed by Spiegel et al. (2009), who parameterized the dynamics in one dimension using eddy diffusion and estimated the eddy-diffusion coefficients needed to keep TiO particles of various sizes lofted. If one translates our vertical velocities into eddy diffusivities by multiplying the vertical velocities by the pressure scale height, then the implied eddy diffusivities at 1 mbar are $\sim 10^{11}\mathrm{cm^2\,sec^{-1}}$. In their HD 209458b model, at 1 mbar, these eddy diffusivities are sufficient to loft particles smaller than several μm. Thus, their calculations likewise suggest that TiO stratospheres may be viable if the TiO particle sizes are less than several μm.

6. CONCLUSIONS

We presented global, three-dimensional numerical simulations of the atmospheric circulation of HD 189733b and HD 209458b that couple the dynamics to a realistic representation of cloud-free nongray radiative transfer. This new model, which we dub SPARC/MITgcm, is the first three-dimensional dynamical model for any giant planet—including those in our solar system—to incorporate nongray radiative transfer. Our model adopts the MITgcm for the dynamics and an optimized version of the radiative model of McKay, Marley, Fortney, and collaborators for the radiative transfer. Opacities are calculated assuming solar composition (or some multiple thereof) with equilibrium chemistry that accounts for rainout. Like earlier work with simplified forcing (Showman et al. 2008a; Cooper & Showman 2005; Showman & Guillot 2002), our simulations develop a broad eastward equatorial jet, mean westward flow at high latitudes, and substantial flow over the poles at low pressure. The jet structure depends significantly on longitude at pressures <100 mbar.

For HD 189733b, our simulations that exclude TiO and VO opacity explain the broad features of the observed 8 and 24 μm light curves (Knutson et al. 2007, 2009), including the modest day–night flux variation and the fact that the planet/star flux ratio peaks before the secondary eclipse. In our simulations, the offset results from the eastward displacement of the hot regions from the substellar point. On the other hand, we do not fit the flux minimum seen after transit in the 8 μm light curve (Knutson et al. 2007). Our simulations also provide reasonable matches to the *Spitzer* secondary-eclipse depths at 4.5, 5.8, 8, 16, and 24 μm (Charbonneau et al. 2008; Deming et al. 2006) and the ground-based upper limit at 2.2 μm from Barnes et al. (2007). The temporal variability in these simulations is modest—of order 1%—and is fully consistent with the upper limit on temporal variability from Agol et al. (2009).

The primary HD 189733b observation where we fare poorly is the 3.6 μm secondary-eclipse depth from Charbonneau et al. (2008), which we underpredict by about a factor of 2. Because the 3.6 μm channel is expected to sense down to ∼0.1–1 bar on this planet (Figure 9, left panel), this suggests that our simulation is too cold in this region of the atmosphere and/or has the incorrect opacity in this wavelength range. Previous one-dimensional models of HD 189733b have suffered a similar problem at this wavelength (Barman 2008; Knutson et al. 2009), as have one-dimensional models of brown dwarfs with similar effective temperatures (Geballe et al. 2009). A full-orbit light curve of HD 189733b at 3.6 μm, possible with warm *Spitzer*, would provide crucial insights to help resolve this problem.

For HD 209458b, we include gaseous TiO and VO opacity to see whether it allows us to explain the inference of a stratosphere from *Spitzer* photometry (Knutson et al. 2008; Burrows et al. 2007; Fortney et al. 2008). As expected, these simulations develop a hot (>2000 K) dayside stratosphere whose horizontal dimensions are small at depth but widen with altitude until the stratosphere covers most of the dayside at pressures <0.1 mbar. Interestingly, both branches of the bifurcation discussed by Hubeny et al. (2003) for different planets occur here on a single planet's dayside. Using the terminology of Fortney et al. (2008), the substellar region is a pM-class planet but the terminators and nightside are a pL-class planet. It is thus perhaps more proper to talk about pM-class *daysides* rather than pM-class *planets*.

But despite the stratosphere in our simulations of HD 209458b, we do not reproduce current *Spitzer* photometry of this planet, which includes particularly high (∼1700–1900 K) brightness temperatures in the 4.5 and 5.8 μm channels. This could mean that our stratosphere has the incorrect properties (e.g., temperature range, altitude range, and vertical thermal gradient). However, a fundamental difficulty in explaining the diverse brightness dayside temperatures (ranging from ∼1500 to 1900 K in *Spitzer* bandpasses) is that the range of pressures from which emergent infrared photons originate are very similar for all *Spitzer* bandpasses, at least as calculated by our radiative model with equilibrium chemistry. This means that *regardless* of the planet's temperature profile, the brightness temperatures in all these bands should be similar. Breaking this degeneracy would require changing the opacities so that the opacities in different *Spitzer* bandpasses differ significantly. Dropping the

equilibrium chemistry assumption would make this possible; this provides a clue that disequilibrium chemistry may be important. Disequilibrium chemistry appears to influence infrared spectra of brown dwarfs (e.g., Leggett et al. 2007; Geballe et al. 2009), lending weight to this possibility.

Our light curves of HD 209458b in *Spitzer* bandpasses exhibit modest day–night variation, and we successfully explain the upper limit on the day–night flux contrast from Cowan et al. (2007) at 8 μm. Our ability to meet this constraint results from the fact that much of the dayside 8 μm radiation emanates from altitudes near the base of the stratosphere, where temperatures are not too hot, while nightside 8 μm radiation emanates from substantially deeper pressures where temperatures are warmer than they are aloft. This dual effect leads to modest day–night flux variations despite large day–night temperature variations (on isobars) at low pressures. Assuming the high inferred 4.5 and 5.8 μm brightness temperatures indeed result from a stratosphere, we suggest that the real planet should exhibit large phase variations at 4.5 and 5.8 μm yet more modest phase variations at other *Spitzer* bandpasses and *K* band.

The task of developing exoplanet GCMs that couple dynamics and radiative transfer has now been espoused by many authors, and the work presented here demonstrates that this approach indeed holds significant promise for explaining atmospheric observations of hot Jupiters. Our three-dimensional SPARC/MITgcm simulations, especially of HD 189733b, show encouraging resemblance to observations of the real planet. While some discrepancies remain, and a wider range of parameters need be explored, these simulations support the idea that detailed model/data comparisons can eventually allow robust inferences about the circulation regime of hot Jupiters to be inferred. Given the huge range in properties of currently known transiting planets, with future observations sure to unveil additional surprises, this helps energize the exciting prospect that planetary meteorology can successfully be extended beyond the confines of our solar system.

This research was supported by NASA Origins grant NNX08AF27G and Planetary Atmospheres grants NNX07AF35G and NNG06GF28G to A.P.S.

REFERENCES

Ackerman, A. S., & Marley, M. S. 2001, ApJ, 556, 872

Adcroft, A., Campin, J.-M., Hill, C., & Marshall, J. 2004, Mon. Weather Rev., 132, 2845

Agol, E., Cowan, N. B., Bushong, J., Knutson, H., Charbonneau, D., Deming, D., & Steffen, J. H. 2009, in Proc. IAU Symp. 253, Transiting Planets, ed. D. Queloz, D. Sasselov, M. Torres, & M. Holman (Cambridge: Cambridge Univ. Press), 209

Arakawa, A., & Lamb, V. 1977, Methods Comput. Phys., 17, 173

Barman, T. 2007, ApJ, 661, L191

Barman, T. S. 2008, ApJ, 676, L61

Barnes, J. R., Barman, T. S., Jones, H. R. A., Leigh, C. J., Collier Cameron, A., Barber, R. J., & Pinfield, D. J. 2008, MNRAS, 390, 1258

Barnes, J. R., Barman, T. S., Prato, L., Segransan, D., Jones, H. R. A., Leigh, C. J., Collier Cameron, A., & Pinfield, D. J. 2007, MNRAS, 382, 473

Burrows, A., Budaj, J., & Hubeny, I. 2008, ApJ, 678, 1436

Burrows, A., Hubeny, I., Budaj, J., Knutson, H. A., & Charbonneau, D. 2007, ApJ, 668, L171

Burrows, A., et al. 1997, ApJ, 491, 856

Chamberlain, J. W., & Hunten, D. M. 1987, Theory of Planetary Atmospheres: An Introduction to Their Physics and Chemistry (Orlando, FL: Academic Press Inc.)

Charbonneau, D., Knutson, H. A., Barman, T., Allen, L. E., Mayor, M., Megeath, S. T., Queloz, D., & Udry, S. 2008, ApJ, 686, 1341

Cho, J. Y.-K., Menou, K., Hansen, B. M. S., & Seager, S. 2003, ApJ, 587, L117

Cho, J. Y.-K., Menou, K., Hansen, B. M. S., & Seager, S. 2008, ApJ, 675, 817

Cooper, C. S., & Showman, A. P. 2005, ApJ, 629, L45

Cooper, C. S., & Showman, A. P. 2006, ApJ, 649, 1048

Cowan, N. B., Agol, E., & Charbonneau, D. 2007, MNRAS, 379, 641

Deming, D., Harrington, J., Seager, S., & Richardson, L. J. 2006, ApJ, 644, 560

Deming, D., Seager, S., Richardson, L. J., & Harrington, J. 2005, Nature, 434, 740

Dobbs-Dixon, I., & Lin, D. N. C. 2008, ApJ, 673, 513

Durran, D. R. 1991, Mon. Weather Rev., 119, 702

Fortney, J. J. 2005, MNRAS, 364, 649

Fortney, J. J., Cooper, C. S., Showman, A. P., Marley, M. S., & Freedman, R. S. 2006a, ApJ, 652, 746

Fortney, J. J., Lodders, K., Marley, M. S., & Freedman, R. S. 2008, ApJ, 678, 1419

Fortney, J. J., & Marley, M. S. 2007, ApJ, 666, L45

Fortney, J. J., Marley, M. S., Lodders, K., Saumon, D., & Freedman, R. 2005, ApJ, 627, L69

Fortney, J. J., Saumon, D., Marley, M. S., Lodders, K., & Freedman, R. S. 2006b, ApJ, 642, 495

Freedman, R. S., Marley, M. S., & Lodders, K. 2008, ApJS, 174, 504

Geballe, T. R., Saumon, D., Golimowski, D. A., Leggett, S. K., Marley, M. S., & Noll, K. S. 2009, ApJ, 695, 844

Goodman, J. 2009, ApJ, 693, 1645

Goody, R. M., & Yung, Y. L. 1989, Atmospheric Radiation: Theoretical Basis (2nd ed.; New York: Oxford Univ. Press)

Grillmair, C. J., Charbonneau, D., Burrows, A., Armus, L., Stauffer, J., Meadows, V., Van Cleve, J., & Levine, D. 2007, ApJ, 658, L115

Guillot, T., Burrows, A., Hubbard, W. B., Lunine, J. I., & Saumon, D. 1996, ApJ, 459, L35

Harrington, J., Hansen, B. M., Luszcz, S. H., Seager, S., Deming, D., Menou, K., Cho, J. Y.-K., & Richardson, L. J. 2006, Science, 314, 623

Held, I. M., & Suarez, M. J. 1994, Bull. Am. Meteorol. Soc., 75, 1825

Hubeny, I., Burrows, A., & Sudarsky, D. 2003, ApJ, 594, 1011

Iro, N., Bézard, B., & Guillot, T. 2005, A&A, 436, 719

Kirk, R. L., & Stevenson, D. J. 1987, ApJ, 316, 836

Knutson, H. A., Charbonneau, D., Allen, L. E., Burrows, A., & Megeath, S. T. 2008, ApJ, 673, 526

Knutson, H. A., et al. 2007, Nature, 447, 183

Knutson, H. A., et al. 2009, ApJ, 690, 822

Langton, J., & Laughlin, G. 2007, ApJ, 657, L113

Langton, J., & Laughlin, G. 2008, ApJ, 674, 1106

Leggett, S. K., Saumon, D., Marley, M. S., Geballe, T. R., Golimowski, D. A., Stephens, D., & Fan, X. 2007, ApJ, 655, 1079

Lian, Y., & Showman, A. P. 2008, Icarus, 194, 597

Lian, Y., & Showman, A. P. 2009, Icarus, submitted

Liu, J., Goldreich, P. M., & Stevenson, D. J. 2008, Icarus, 196, 653

Lodders, K. 2002, ApJ, 577, 974

Lodders, K., & Fegley, B. 2002, Icarus, 155, 393

Lodders, K., & Fegley, B., Jr. 2006, in Astrophysics Update, Vol. 2, ed. J. W. Mason (Chichester: Praxis Publishing), 1

Lubow, S. H., Tout, C. A., & Livio, M. 1997, ApJ, 484, 866

Machalek, P., McCullough, P. R., Burke, C. J., Valenti, J. A., Burrows, A., & Hora, J. L. 2008, ApJ, 684, 1427

Marley, M. S., Gelino, C., Stephens, D., Lunine, J. I., & Freedman, R. 1999, ApJ, 513, 879

Marley, M. S., & McKay, C. P. 1999, Icarus, 138, 268

Marley, M. S., Saumon, D., Guillot, T., Freedman, R. S., Hubbard, W. B., Burrows, A., & Lunine, J. I. 1996, Science, 272, 1919

Marley, M. S., Seager, S., Saumon, D., Lodders, K., Ackerman, A. S., Freedman, R. S., & Fan, X. 2002, ApJ, 568, 335

McKay, C. P., Pollack, J. B., & Courtin, R. 1989, Icarus, 80, 23

Menou, K., Cho, J. Y.-K., Seager, S., & Hansen, B. M. S. 2003, ApJ, 587, L113

Peixoto, J. P., & Oort, A. H. 1992, Physics of Climate (New York: AIP)

Pont, F., Knutson, H., Gilliland, R. L., Moutou, C., & Charbonneau, D. 2008, MNRAS, 385, 109

Redfield, S., Endl, M., Cochran, W. D., & Koesterke, L. 2008, ApJ, 673, L87

Rhines, P. B. 1975, J. Fluid Mech., 69, 417

Richardson, L. J., Deming, D., Horning, K., Seager, S., & Harrington, J. 2007, Nature, 445, 892

Salby, M. L. 1996, Fundamentals of Atmospheric Physics (San Diego: Academic Press)

Saumon, D., & Marley, M. S. 2008, ApJ, 689, 1327

Scott, R. K., & Polvani, L. 2007, J. Atmos. Sci., 64, 3158

Scott, R. K., & Polvani, L. M. 2008, Geophys. Res. Lett., 35, 24202
Showman, A. P. 2007, J. Atmos. Sci., 64, 3132
Showman, A. P. 2008, Nature, 452, 296
Showman, A. P., Cooper, C. S., Fortney, J. J., & Marley, M. S. 2008a, ApJ, 682, 559
Showman, A. P., & Guillot, T. 2002, A&A, 385, 166
Showman, A. P., Menou, K., & Cho, J. Y.-K. 2008b, in ASP Conf. Ser. 398, Extreme Solar Systems, ed. D. Fischer et al. (San Francisco, CA: ASP), 419
Sing, D. K., Vidal-Madjar, A., Lecavelier des Etangs, A., Desert, J. M., Ballester, G., & Ehrenreich, D. 2008, ApJ, 686, 667
Spiegel, D. S., Silverio, K., & Burrows, A. 2009, ApJ, in press (arXiv:0902.3995)
Swain, M. R., Bouwman, J., Akeson, R., Lawler, S., & Beichman, C. 2008a, ApJ, 674, 482
Swain, M. R., Vasisht, G., & Tinetti, G. 2008b, Nature, 452, 329
Tinetti, G., et al. 2007, Nature, 448, 169
Toon, O. B., McKay, C. P., Ackerman, T. P., & Santhanam, K. 1989, J. Geophys. Res., 94, 16287
Vasavada, A. R., & Showman, A. P. 2005, Rep. Prog. Phys., 68, 1935
Zahnle, K., Marley, M. S., Lodders, K., & Fortney, J. J. 2009, ApJ, submitted (arXiv:0903.1663)